minerals

MDPI

Article

Integrated Aeromagnetic and Aeroradiometric Analysis for Structural Mapping and Mineral Prospectivity Assessment Using Euler Deconvolution and Fuzzy Logic: A Case Study from the Jabal Gasus Area, Central Eastern Desert, Egypt

Mostafa Nagy [1], Ahmed M. Eldosouky [2,3], El Saeed R. Lasheen [4], Mohamed Salaheldin [5], Saulo P. Oliveira [6,*], Hasan Arman [7], Mabrouk Sami [7,8] and Fathy Abdalla [9,*]

[1] Geology Department, Faculty of Science, Kafrelsheikh University, Kafrelsheikh P.O. Box 33516, Egypt; mostafa_fadila@sci.kfs.edu.eg
[2] Department of Geology, Faculty of Science, Suez University, Suez P.O. Box 43221, Egypt; dr_a.eldosoky@yahoo.com or ahmed.eldosouky@sci.suezuni.edu.eg
[3] Geology of Petroleum and Natural Gas Program, Faculty of Science, Suez National University (SNU), Suez P.O. Box 43221, Egypt
[4] Geology Department, Faculty of Science, Al-Azhar University, Cairo, P.O. Box 11884, Egypt; elsaeedlasheen@azhar.edu.eg
[5] Geology Department, Faculty of Science, Alexandria University, Alexandria, P.O. Box 21511, Egypt; mohamed.salaheldin1089@gmail.com
[6] Graduate Program in Geology and Department of Mathematics, Federal University of Paraná, Curitiba 81531-980, Brazil
[7] Geosciences Department, College of Science, United Arab Emirates University, Al Ain 15551, United Arab Emirates; harman@uaeu.ac.ae (H.A.); mabrouksami@uaeu.ac.ae (M.S.)
[8] Geology Department, Faculty of Science, Minia University, El-Minia P.O. Box 61519, Egypt
[9] College of Science, King Saud University, Riyadh 11451, Saudi Arabia
* Correspondence: saulopo@ufpr.br (S.P.O.); fabdalla@ksu.edu.sa (F.A.)

Abstract

The global increase in demand for critical minerals necessitates efficient exploration approaches that reduce environmental impact while maximizing the discovery of potential mineral deposits. This study aims to (i) delineate magnetic lineaments and lithological boundaries in the Jabal Gasus area, Central Eastern Desert, Egypt; (ii) estimate magnetic-source locations and depths under alternative source-geometry assumptions; and (iii) integrate structural, radiometric, and lithological evidence to delineate and rank zones favorable for structurally controlled gold-polymetallic and intrusion-related mineralization. To achieve these objectives, airborne magnetic and radiometric data were analyzed using Improved Logistic (IL) and Logsigm Function (LSF) edge-detection filters, Euler deconvolution (EUD), Center for Exploration Targeting (CET) grid and porphyry analyses, and GIS-based fuzzy logic modeling. The results identify N-S, NW-SE, and NE-SW magnetic lineaments and structural corridors that are spatially associated with lithological contacts, intrusive features, and known mineral occurrences. Euler deconvolution provides model-dependent estimates of source location and depth under alternative assumed source geometries; these estimates are used as supporting structural constraints rather than as uniquely resolved fault depths. Radiometric signatures, including high potassium, anomalous eU concentrations, and high F-parameter values, primarily reflect lithological contrasts and identify areas for follow-up assessment of possible hydrothermal alteration where supported by independent geological evidence. The integrated fuzzy prospectivity model provides a knowledge-driven, first-pass ranking of areas for follow-up exploration.

Academic Editor: Stanislaw Mazur

Received: 16 September 2026
Revised: 20 October 2026
Accepted: 20 October 2026
Published: 23 October 2026

Copyright: © 2026 by the authors. Licensee MDPI, Basel, Switzerland. This article is an open access article distributed under the terms and conditions of the Creative Commons Attribution (CC BY) license.

The highly favorable class covers 62.53% of the area and contains five of seven known hydrothermal occurrences, indicating regional selectivity. The AUC of 0.733 is an internal success-rate estimate, without independent testing or spatial cross-validation. This study presents the first integrated magnetic–radiometric–fuzzy logic mineral system model developed for the Jabal Gasus district, resolving a depth structural framework and a prospectivity map that were not available from prior investigations of the area. This methodology indicates that integrated geophysical investigation helps manage exploration uncertainty, establishing an applicable workflow for sustainable mineral exploration in the ENS and similar Precambrian terrains.

Keywords: Jabal Gasus; mineralized granites; aeromagnetic data; radiometric data; high-precision edge detection; fuzzy logic model

1. Introduction

Increasing worldwide demand for mineral commodities has strengthened the need for resource-development practices that reconcile supply security with environmental protection. The Eastern Desert of Egypt hosts a wide spectrum of mineral deposits distributed over a vast geological domain. From a tectonostratigraphic perspective, the region constitutes part of the Arabian–Nubian Shield (ANS), a prominent Precambrian terrane characterized by extensive igneous and metamorphic rock assemblages [1]. The ANS comprises ancient crystalline basement rocks, including granites, gneisses, and schists, that record a complex history of tectonic deformation, magmatism, and crustal evolution. During the Neoproterozoic, the region underwent intense volcanic and plutonic activity, which played a fundamental role in the formation and localization of economically significant mineralization, notably gold, molybdenum, and other polymetallic (Cu-Pb-Zn) metals [1,2].

The evolution of the ANS during the Pan-African Orogeny provides an important framework for investigating processes related to continental crust formation. The Eastern Desert of Egypt exposes a Precambrian basement assemblage comprising volcanic, plutonic, and sedimentary rocks. These lithologies record different intensities of deformation and metamorphic reworking and are separated from the overlying Cretaceous sedimentary succession by an unconformity. The final stages of magmatic activity were marked by the emplacement of post-orogenic alkali granites and contemporaneous dyke swarms during episodes of crustal extension that affected large parts of the Eastern Desert and Central Arabia toward the close of the Pan-African Orogeny [3,4].

In this regional tectonic context, Wadi Gasus is a structurally complex sector in which ancient mine workings are spatially associated with NE-striking quartz veins that cut biotite granite and metavolcanic country rocks [5]. These mineral assemblages constitute a significant component of the ANS basement complex [3]. This study addresses the existing knowledge gap by applying a geophysical processing technique to magnetic and radiometric datasets to delineate the subsurface structural architecture and target areas favorable for mineralization. The study applies integrated geophysical processing to delineate structural architecture and rank areas that warrant follow-up mineral exploration. Integrating structural, lithological, and radiometric information may improve early-stage target prioritization; however, the present study does not quantify reductions in exploration cost, drilling, risk, or environmental disturbance [6,7].

Airborne magnetic surveying is widely recognized as an effective geophysical technique for mineral exploration because it enables rapid, non-invasive, and cost-efficient investigation of subsurface features over large areas. The method is particularly valuable

for detecting concealed mineral deposits, delineating basement architecture, mapping lithological contacts and structural discontinuities, and identifying magnetic anomalies associated with mineralization [8–13]. Its utility is especially pronounced in terrains containing magnetite and other magnetic minerals, where variations in the Earth's magnetic field can reveal the geometry of magnetic sources and provide important constraints on the structural controls of ore formation [6,7]. In geologically complex regions, aeromagnetic data can therefore provide critical subsurface information that may not be resolved adequately by conventional exploration methods. Nevertheless, interpretation of magnetic data may be complicated by overlapping anomalies, variable source depths, and structurally intricate settings, all of which can introduce uncertainty into geological models [14,15]. Recent advances in sensor technology, acquisition strategies, high-resolution datasets, and integrated geological constraints have significantly improved the reliability and interpretability of airborne magnetic data, thereby enhancing its role in mineral prospectivity assessment and exploration targeting [16–18].

Progress in magnetic-data analysis has improved substantially, leading to the development of numerous filtering, modeling, and edge-enhancement techniques. Common edge detectors, including total gradient amplitude [19], tilt derivative [20], total gradient [21], and enhanced total gradient [22], are widely applied to delineate geological contacts. However, they commonly emphasize shallow-source anomalies [23]. To improve the balance between shallow and deeper responses, additional methods such as theta mapping [24], the gradient amplitude of the tilt derivative [25], and the normalized horizontal derivative have been introduced [26]. Nevertheless, these filters may still generate spurious or non-geological lineaments in structural interpretations [23]. In this context, the Center for Exploration Targeting (CET) grid analysis [27] provides a more robust framework for integrating magnetic responses with geological information, thereby enhancing the reliability of structural mapping and mineral-prospect targeting [9].

Airborne Radiometric surveying is a robust and widely utilized geophysical technique essential for mineral exploration, geological mapping, and environmental monitoring [28]. The method operates by quantifying the abundance of naturally occurring potassium (K), equivalent uranium (eU), and equivalent thorium (eTh) based on their distinct spectral emissions [29]. From a geological perspective, mapping the distribution of these radioelements provides critical constraints on magmatic evolution, rock petrogenesis, and crustal geodynamics. It also serves as a powerful vectoring tool in mineral exploration, helping to delineate hydrothermal alteration and zones of high mineralization potential [30].

The study area is considered a geologically promising domain for mineral exploration, with previous geological and geophysical investigations documenting the presence of economically significant mineralization [1–3,31,32]. In this study, high-resolution aeromagnetic and radiometric data were integrated with advanced processing and interpretation techniques, including high-precision edge detection, CET-GA grid analysis [27], and the CET-PA Porphyry approach [33], to delineate previously unresolved structural fabrics and alteration patterns associated with mineralization. This integrated workflow enabled the generation of comprehensive structural maps and the identification of prospective metallogenic targets, particularly within the study area, while also establishing a transferable strategy for prospect-scale exploration in comparable mineralized terranes. In addition, the Euler deconvolution (EUD) [34] technique was applied to estimate the depths of causative geological structures, as such methods are widely used in early-stage magnetic interpretation for providing efficient and practical constraints on subsurface geometry.

Although the aeromagnetic expression of the Gasus area has previously been examined by Zaki et al. [5], that study relied on qualitative magnetic filtering and two-dimensional forward modeling along discrete profiles to estimate depth to basement, without

incorporating radiometric data, high-precision edge detection, or a quantitative targeting product. Nagy and Eldosouky [35] subsequently applied a broadly comparable integrated geophysical–radiogenic workflow; however, that study addressed pluton-hosted rare-earth-element mineralization at Jabal Umm Naggat, a mineral system that differs fundamentally in commodity, host lithology, and structural setting from the district-scale, structurally controlled polymetallic system examined here. The study targets structurally controlled hydrothermal mineralization of the type that characterizes the Eastern Desert: shear-zone-hosted (orogenic) gold in quartz and quartz-carbonate veins and associated polymetallic (Cu-Pb-Zn) vein-type mineralization, formed during the Neoproterozoic orogeny and controlled by brittle-ductile shear zones of the Najd system and later reactivated structures [3,4]. A secondary, exploratory target is intrusion-related (porphyry-style) mineralization, represented by the district's molybdenum and polymetallic occurrences [32]. Syn-sedimentary phosphate in the Duwi Formation was excluded from model evaluation. Following the mineral systems, the evidence layers were selected to represent (i) fluid pathways and structural architecture, (ii) host rocks and structural or lithological traps, (iii) intrusive centers as possible heat and fluid sources, and (iv) a possible hydrothermal footprint. The present study addresses this gap by (i) jointly integrating aeromagnetic and aeroradiometric datasets for the Jabal Gasus district for the first time, (ii) applying a three-index Euler deconvolution (SI = 0, 0.5, and 1) together with CET-GA and CET-PA analyses to resolve a spatially continuous, depth-structural framework extending below 2 km, and (iii) generating a fuzzy logic prospectivity map for structurally controlled gold-polymetallic and intrusion-related mineralization, with each evidence layer linked to a component of the deposit model, not previously available for this district.

2. Geological Setting

The study area is situated south of Port Safaga in the northern segment of the Central Eastern Desert (Figure 1a,b). The geomorphology of the region is dominated by a series of mountainous ridges of varying elevations, notably Jabal Gasus (466 m), Jabal Um al Huweitat (427 m), Jabal Wasif (898 m), and Jabal Weira (621 m). This elevated topography is intersected by major drainage systems, such as Wadi Safaga, Wadi Gasus, Wadi Wasif, and Wadi Saqi, which are filled with undifferentiated Quaternary alluvial sediments. The study area comprises a broad lithological diversity, including igneous, metamorphic, and sedimentary sequences varying in age from Precambrian to Quaternary (Figure 1c).

The Precambrian basement complex of the Eastern Desert of Egypt has been the subject of several classification schemes [36–39]. Within the study area, these Precambrian rocks occupy approximately 70% of the total area (Figure 1c). Lithostratigraphically, the main basement units, in ascending chronological order, are serpentinite, ophiolitic metagabbro, metagabbro-diorite complex, metavolcanics, Hammamat sediments, metasediments, gabbroic rocks, older granites, younger granites, Dokhan volcanics, and post-Hammamat felsites. The sedimentary successions in the study area range in age from Cretaceous to Quaternary and rest unconformably on Precambrian basement rocks. They include, in chronological order, the Taref, Duwi, Dakhla, Tarwan, Esna, Thebes, Nakheil, Umm Gheig, Umm Mahara, and Shagra formations. Of these units, the Duwi Formation is of particular importance because it is composed mainly of phosphate beds intercalated with marl, black shale, and oyster limestone. The phosphate deposits have been the subject of extensive geological and radiometric investigations, many of which have confirmed the presence of economically valuable uranium concentrations [40–42]. Quaternary sediments constitute the youngest surficial deposits in the study area and consist of detritus, sand, gravel, pebbles, cobbles, and boulders. They occur throughout the area and form the surface cover within the principal drainage channels, including Wadi Gasus, Wadi

Safaga, and Wadi Saqi. These deposits originated from the weathering and erosion of the diverse rock units exposed across the region.

Structurally, the Wadi Gasus district occupies the intersection of two contrasting tectonic regimes—the Pan-African, NE-trending Najd-type sinistral shear corridor system [43] and the younger Oligo-Miocene Red Sea rift—which overprinted the inherited basement fabric with NW-trending normal faults and NNE-trending sinistral transfer zones. This composite tectonic evolution generated a reactivated, kinematically heterogeneous brittle–ductile fault network that channeled episodic hydrothermal-fluid flow and promoted polymetallic mineralization [44]. The district is also characterized by phosphate, gold, molybdenum, and other polymetallic ore deposits [32].

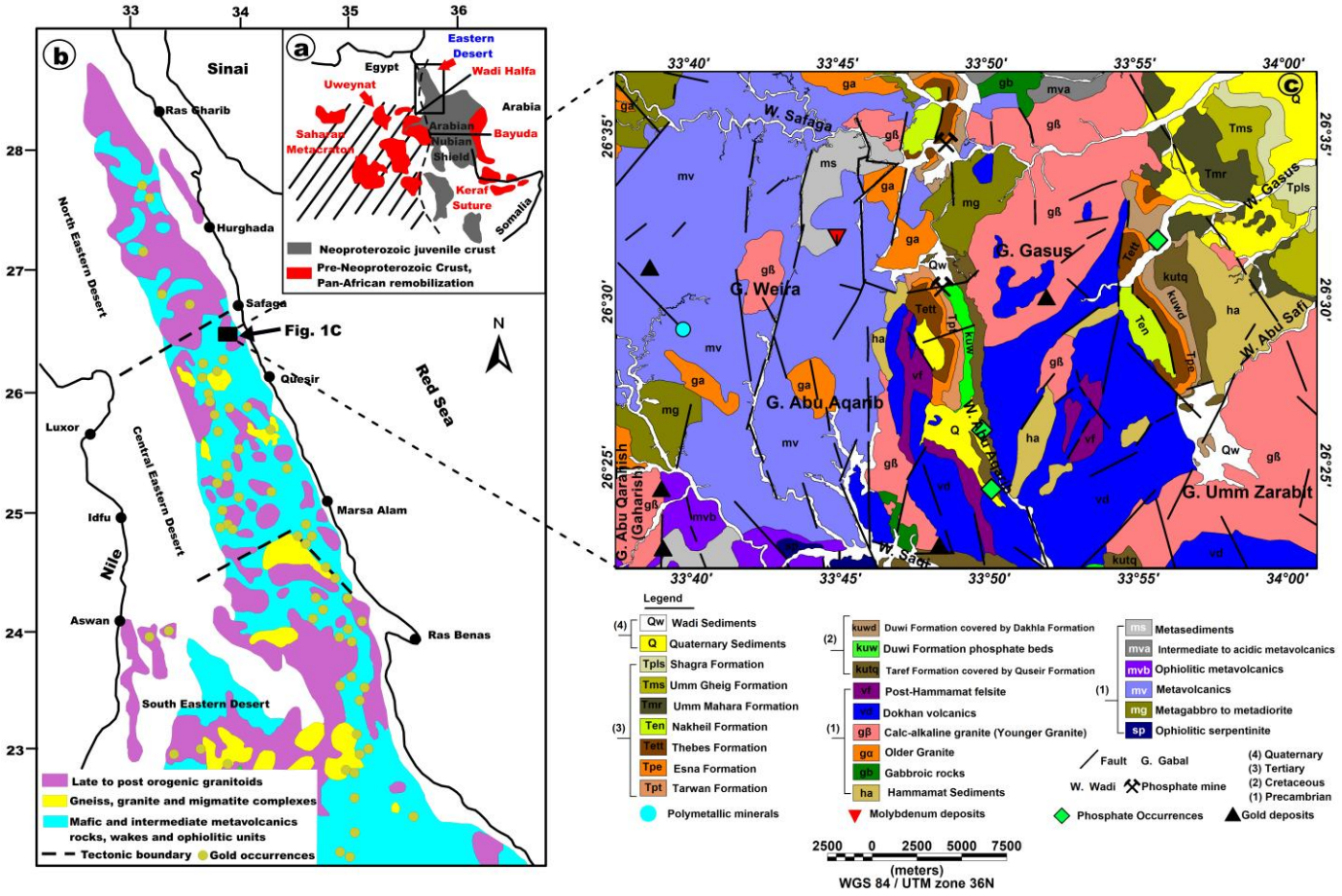


Figure 1. (**a**) Regional location of the Arabian–Nubian Shield (ANS). (**b**) Classification of the Precambrian basement exposed in Egypt's Eastern Desert into northeastern, central, and southeastern sub-provinces. (**c**) Simplified geological map of the Jabal Gasus district (modified after [45]); black triangles = gold, red inverted triangles = molybdenum, cyan circle = polymetallic (Cu-Pb-Zn), green diamonds and crossed hammers = phosphate occurrences and mines.

3. Materials and Methods

3.1. Aeromagnetic Data

The study used processed total magnetic intensity (TMI) data from the regional airborne magnetic–radiometric survey conducted by the Aero-Service Division of Western Geophysical Company of America for the Egyptian General Petroleum Corporation and the Egyptian Geological Survey and Mining Authority, 1984 [46]. Traverse lines were oriented NE–SW, approximately 45°/225° from true north, whereas tie lines were oriented NW–SE, approximately 135°/315°, with terrain clearance of 120 m, 10 km tie-line spacing,

and traverse-line spacing of 1.0 km in different survey blocks. The original regional survey employed a Varian V-85 proton-precession magnetometer (Varian Associates, Palo Alto, CA, USA). The present study used the archived processed TMI grid rather than raw flight-line observations. The survey geometry is given schematically in Supplementary Figure S1. The TMI grid was transformed by reduction to the pole (RTP) in the Fourier domain [47]. RTP was calculated using an inducing-field inclination of 32.8° and a declination of 1.9°. The grid was generated with 250 m cells (minimum curvature; WGS 84/UTM Zone 36N) before RTP transformation.

3.1.1. High-Precision Edge Detection

Edge detection approaches have become fundamental tools in geophysical interpretation for defining structural discontinuities, including faults, contacts, dykes, and mineralized corridors [9,10,48–51]. The Improved Logistic (IL) [23,52] and Logsigm Function (LSF) [53] filters were applied to the RTP, 1 km, and 2 km upward-continued grids to enhance magnetic-source boundaries.

(i) Improved logistic (IL) filter.

The IL method, proposed by Pham et al. [23], applies a logistic transformation to the analytical signal, following the earlier formulation of Pham et al. [52], to normalize and enhance contrast among signals of different amplitudes. This approach was further applied by Eldosouky et al. [9] for high-resolution structural mapping using potential-field and remote-sensing data. It is expressed as follows:

$$\boldsymbol{IL} = \frac{\mathbf{1}}{\mathbf{1} + \exp(-\boldsymbol{K}(\boldsymbol{R_{THDR}} - \mathbf{1}) + \mathbf{1})} \quad (1)$$

where

$$\boldsymbol{R_{THDR}} = \frac{\frac{\boldsymbol{\partial THDR}}{\boldsymbol{\partial z}}}{\sqrt{\left(\frac{\boldsymbol{\partial THDR}}{\boldsymbol{\partial x}}\right)^2 + \left(\frac{\boldsymbol{\partial THDR}}{\boldsymbol{\partial y}}\right)^2}} \quad (2)$$

The improved logistic (IL) filter was applied to the RTP, 1 km upward-continued RTP, and 2 km upward-continued RTP grids using K = 2.

(ii) Logsigm function of the Horizontal Gradient (LSF) filter.

The LSF represents an advanced edge-detection technique that improves the interpretation of potential-field data and the mapping of geological boundaries [53]. The LSF [53] is expressed as:

$$\boldsymbol{LSF} = \left(\frac{\mathbf{1}}{\mathbf{1} + \exp(-\boldsymbol{kernel_R})}\right)^{\boldsymbol{2+Range}} \quad (3)$$

where

$$\boldsymbol{kernel_R} = [\boldsymbol{K}(\boldsymbol{R_{THDR}})] - \boldsymbol{\pi/4} \quad (4)$$

The parameter *K* was assigned values between 0.5 and 3, and a value of 3 was adopted in the present study.

3.1.2. Euler Depth Estimation Method (EUD)

Euler deconvolution [34,54] was applied to the RTP grid to estimate magnetic-source locations and depths under alternative source-geometry assumptions, using the homogeneity equation:

$$\frac{\boldsymbol{\partial T}}{\boldsymbol{\partial x}}(\boldsymbol{x} - \boldsymbol{x_0}) + \frac{\boldsymbol{\partial T}}{\boldsymbol{\partial y}}(\boldsymbol{y} - \boldsymbol{y_0}) + \frac{\boldsymbol{\partial T}}{\boldsymbol{\partial z}}(\boldsymbol{z} - \boldsymbol{z_0}) = \mathbf{SI}(\boldsymbol{B} - \boldsymbol{T}) \quad (5)$$

In this formulation, SI denotes the structural index, which describes the geometry of the causative source; B represents the regional or background magnetic field; and T is the magnetic-field value measured at the coordinates (x, y, z). Euler deconvolution was applied to the RTP magnetic grid using Oasis Montaj v8.4. Structural indices of 0.0, 0.5, and 1.0 were assigned to contact-like, dyke-like, and fault-like source geometries, respectively. Calculations used a 10 × 10-cell moving window. Solutions were grouped into five depth classes (<500 m, 500–1000 m, 1000–1500 m, 1500–2000, and >2000 m) and spatially clustered, retaining only clusters supported by five or more solutions within a 500 m radius, to reduce the influence of scattered or spurious solutions on the interpreted depth architecture.

3.1.3. CET Grid Analysis

CET Grid Analysis [27,33,55] was applied using a 5-cell standard-deviation filter. Ridge features were then extracted via Phase Symmetry detection, configured with a minimum filter wavelength of 5 cells, 5 filter scales, and a symmetry robustness parameter of 3; the analysis was constrained to positive-amplitude anomalies only. To convert these ridges into vector form, we applied Amplitude Thresholding at a cutoff of mean plus two standard deviations, generating ridges with an output width of 5 cells, and then performed Skeletonization followed by Skeleton-to-Vector conversion under default parameter settings. Junction density, used here as a proxy for structural complexity, was calculated by lowering the contact-voting influence to 3, which sharpens the detection of discrete lineament intersections. Lineament density was subsequently computed from the combined derived lineament datasets using a line-density algorithm.

3.1.4. CET Porphyry Analysis

CET Porphyry Analysis (CET-PA) [56] was applied to detect circular magnetic features. The Circular Feature Transform (CFT) was run with radii ranging from 3 to 21 cells in increments of 2, using the Mean calculation method and a circularity constraint of 2.0. We then applied Central Peak Detection over a threshold range of 5 to 15 in 5-unit increments, using a 6-cell exclusion radius around each detected peak, and restricted the search to elevation (positive-amplitude) features only. Separately, the Amplitude Contrast Transform was calculated over radii ranging from 3 to 11 cells in 2-cell increments, using the Mean Contrast method. These identical parameter settings were replicated across the RTP, UC-1 km, and UC-2 km grids to ensure consistency in the resulting outputs.

3.2. Airborne Radiometric Data

The radiometric data were acquired in the same airborne program and flight configuration as the magnetic data (Section 3.1). Airborne radiometric data support lithological mapping and regional exploration screening. Elevated potassium may reflect primary K-bearing minerals or, where independently documented, hydrothermal K addition involving minerals such as sericite and illite [57]. Alternatively, an RGB ternary image displays potassium in the red channel, thorium in the green channel, and uranium in the blue channel to compare their spatial distributions. The F parameter, expressed as K× (eU/eTh), combines potassium abundance with the eU/eTh ratio and highlights radiometric contrasts that may arise from lithological variation or radioelement redistribution [58,59]. It is therefore used as a complementary screening indicator rather than as a diagnostic measure of potassic alteration or mineralization. Alteration-related interpretations require supporting geological, mineralogical, or geochemical evidence beyond radiometric anomalies and their spatial overlap with magnetic features. Potassium deviation (Kd) was calculated to express the departure of observed potassium from the potassium value expected for the local thorium abundance. The Kd is expressed as:

$$K_d = \left(\frac{K - K_n}{K_n}\right) \quad (6)$$

where

$$K_n = \left(\frac{Kgrid_{average}}{eThgrid_{average}}\right) \times eThMap \quad (7)$$

This provides useful insight into subsurface geology by revealing potassium variability, delineating hydrothermal alteration zones, and pinpointing zones of mineralization potential, which together assist in identifying viable exploration targets [60].

3.3. Fuzzy Logic Modeling

A GIS-based fuzzy logic model integrated four evidence layers: magnetic lineament density, the F-parameter, CET circular-feature scores, and lithology. Continuous inputs were converted to increasing linear membership values (0–1), and lithological units received fixed expert-assigned scores (Supplementary Tables S1 and S2). Layers were equally weighted and combined using the fuzzy gamma operator [61-63]. In the present study, this fuzzy logic framework was applied to combine multiple thematic layers for the generation of a mineral prospectivity map.

The methodological framework is structured into three principal stages. First, fuzzification converts each input layer into fuzzy-membership values using a linear membership function. This procedure places all datasets on a common scale from 0 to 1, allowing them to be integrated consistently. The resulting fuzzy layers are then combined with a suitable fuzzy operator to generate a composite map of mineralization potential or hazard intensity. The gamma operator is frequently selected because it provides a balance between the restrictive behavior of the fuzzy AND operator and the more permissive behavior of the fuzzy OR operator, making it particularly suitable for prospectivity modeling [63]. This operator effectively integrates the characteristics of both the fuzzy algebraic product and the fuzzy algebraic sum into a single output, providing a flexible and moderated aggregation of input evidence. The fuzzy algebraic product typically yields lower membership values, reflecting a conservative or diminishing response, whereas the fuzzy algebraic sum produces comparatively higher values, indicative of an amplifying effect. In the final stage, defuzzification, the aggregated fuzzy output is converted into a single crisp value, enabling straightforward interpretation and supporting informed decision-making [63]. A gamma value of 0.90 was selected based on the sensitivity analysis, which yielded the highest success-rate AUC against the known hydrothermal occurrences among the tested values (0.70, 0.80, 0.90), rather than on visual assessment. Furthermore, this selection promotes a smooth transition between high- and low-response zones, improving the model's sensitivity to mineralization-related signals while minimizing the influence of noise and less relevant features [62,63]. Magnetic lineament density was converted to fuzzy membership values using a linear function, with the lower bound fixed at 0 m/km² (membership value of 0) and the upper bound fixed at 7.08 m/km² (membership value of 1). For the F parameter map, we again used an increasing linear membership function and CFT circular-anomaly grids. The lithology layer was not fuzzified through a continuous function; instead, it was reclassified into categories based on expert judgment of established host-rock associations. Once fuzzified, all four evidence layers were assigned equal weight and integrated using the fuzzy gamma operator with a gamma value of 0.90. All evidence layers were standardized to fuzzy memberships from 0 to 1 (Supplementary Table S1). Continuous F-parameter and CET-PA circular-feature inputs were linearly rescaled between defined lower and upper limits, whereas nominal geological units received fixed-based scores (Supplementary Table S2). Supplementary Table S3 summarizes all datasets and derived parameters used in the study, including those used only for

interpretation, and their roles in the workflow. Dependence among partly correlated alteration, structural, and aeromagnetic inputs was addressed by within-group fuzzy-gamma integration; thus, the final map represents a knowledge-driven favorability ranking, not an independent validation or probability of mineralization.

The ROC curve was constructed by treating the continuous fuzzy-overlay output as a prospectivity score and the locations of the seven documented hydrothermal (gold, molybdenum, and polymetallic) occurrences as the "positive" class. Phosphate occurrences were excluded from the positive class because they are syn-sedimentary and are not the target of the model. For each of a series of threshold values spanning the full range of fuzzy scores, cells above the threshold were classified as predicted prospective and cells below as predicted non-prospective. The true-positive rate (proportion of known occurrences correctly falling within predicted-prospective cells) and false-positive rate (proportion of non-occurrence area incorrectly classified as prospective) were computed at each threshold and plotted against one another to generate the ROC curve. The area under this curve (AUC) summarizes overall discriminatory performance, with AUC = 1.0 indicating perfect discrimination and AUC = 0.5 indicating performance no better than random classification.

4. Results

Regions characterized by structural and lithological complexity are commonly linked to enhanced mineralization potential, although the nature and strength of this relationship depend on the prevailing rock types and tectonic setting [6]. This association is clearly demonstrated in Egypt's Central Eastern Desert (Figure 1c), a geologically intricate terrain that serves as a representative example of such mineral prospectivity. The RTP transformation of the TMI dataset (Figure 2b) generates a magnetic field in which anomalies are distributed symmetrically with respect to their causative source bodies, thereby facilitating direct geological interpretation [64,65]. The RTP magnetic map (Figure 2b) reveals a highly heterogeneous magnetic field characterized by pronounced spatial variability in anomaly intensity and distribution across the study area. Magnetic values range from strongly negative anomalies (−338 nT) to high magnetic responses exceeding 1100 nT, indicating significant contrasts in the magnetic properties of the underlying lithologies. High-amplitude magnetic anomalies (red to pink zones) are predominantly concentrated in the central, southwestern, and northwestern sectors, particularly around Jabal Gasus, Wadi Gasus, and east Jabal Abu Qarahish.

In contrast, low magnetic anomalies (blue to cyan zones) are well developed in the western and southeastern parts of the area, notably around Jabal Weira and Jabal Umm Zarabit. These zones indicate weakly magnetized lithologies that largely coincide with metavolcanic, metasedimentary, and ophiolitic domains. A notable spatial correlation is observed between magnetic anomalies and known mineral occurrences. Gold deposits (black triangles) are frequently associated with moderate to high magnetic gradients, particularly along structural corridors near Jabal Gasus and Wadi Abu Agarib. Similarly, molybdenum and polymetallic occurrences show an affinity with intermediate to high magnetic responses, suggesting a genetic link with magnetically susceptible host rocks or intrusive systems. Phosphate occurrences, however, tend to coincide with relatively moderate to low magnetic signatures, reflecting their association with less magnetic lithologies.

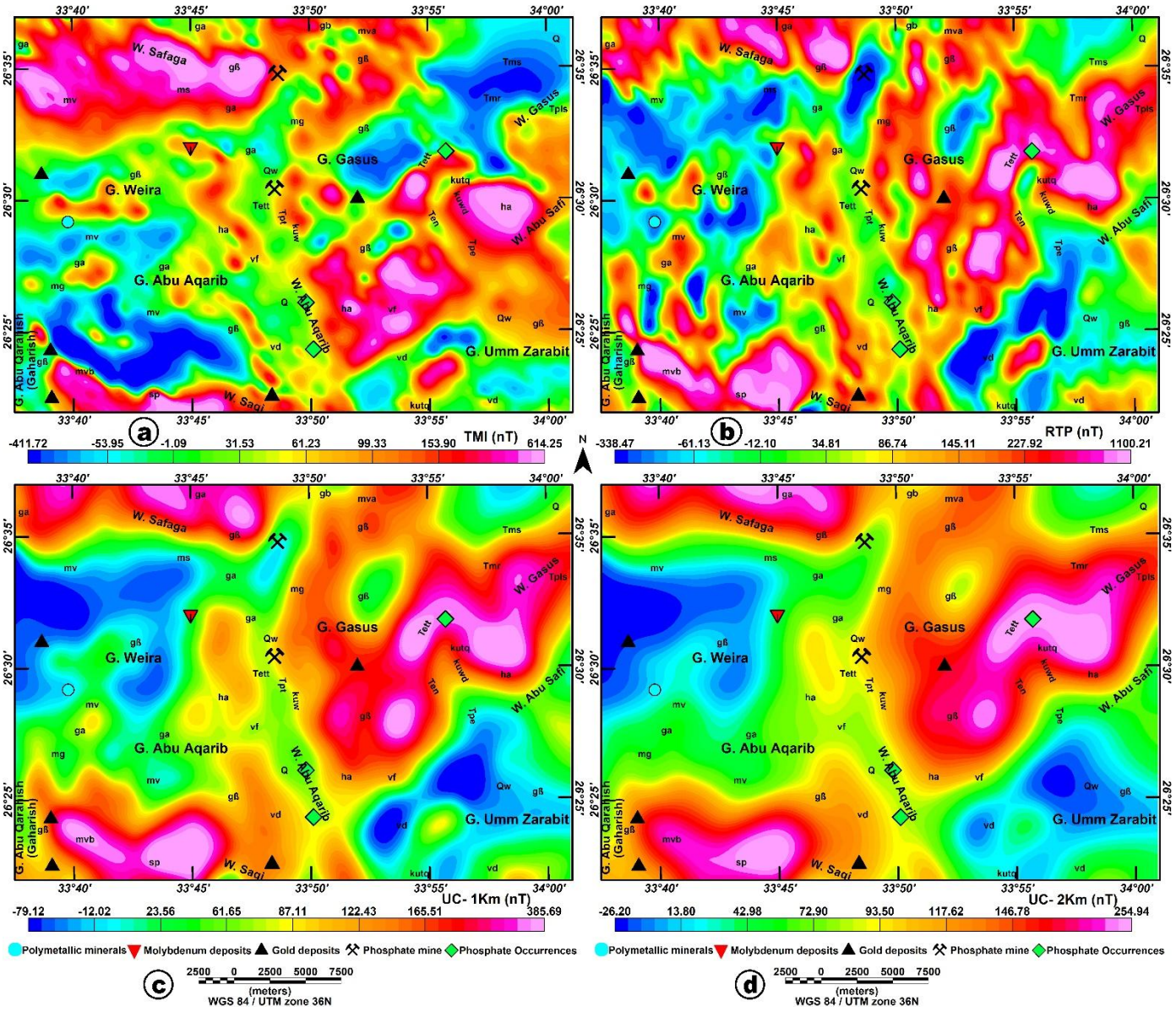


Figure 2. Magnetic anomaly maps of the study area: (**a**) TMI map; (**b**) RTP map; (**c**) UC-RTP at a 1 km scale; (**d**) UC-RTP at a 2 km scale. Mineral occurrence symbols as in Figure 1.

Figure 2c,d present the upward continuation (UC) maps at elevations of 1 km and 2 km, respectively. These transformations were applied to enhance the interpretation of the depth and structural trends of the basement features. The effective investigation depths corresponding to these continuation levels are approximately 0.5 km and 1.0 km, respectively. This observation is consistent with the commonly accepted rule that upward continuation to a height z reflects sources at depths of about z/2 [66–68]. We emphasize that this is a commonly used approximation rather than a precise depth calculation, and for quantitative depth attribution, we rely instead on independent depth solutions derived from Euler deconvolution. The upward continuation maps at 1 km and 2 km reveal a progressive attenuation of short-wavelength magnetic anomalies and a corresponding enhancement of broader regional features. At 1 km continuation, the magnetic map still retains much of the anomaly pattern observed in the RTP data, although several high-frequency anomalies have already been dampened. The main magnetic highs remain prominent in the central, southwestern, and northwestern sectors, particularly around Jabal Gasus, Wadi Gasus corridor, and east Jabal Abu Qarahish, where strong positive responses persist. These features suggest the presence of magnetically susceptible bodies at

moderate depth. In contrast, the western and southeastern sectors continue to exhibit subdued magnetic responses, especially around Jabal Weira and Jabal Umm Zarabit, indicating weakly magnetized lithologies or altered zones.

At 2 km continuation, the map becomes markedly smoother, and most of the localized anomalies seen in the RTP and 1 km products are significantly reduced. The remaining magnetic pattern is dominated by broad regional highs and lows, indicating that the deeper magnetic sources exert the primary control on the observed field at this scale. The central, southwestern, and northwestern high anomaly zone remains well defined, whereas the western magnetic low persists as a large regional feature. This suggests a major lithological contrast across the study area, possibly reflecting differences between magnetic intrusive bodies and less magnetic country rocks. The persistence of these broad anomalies at the 2 km upward-continuation level indicates that they are generated by sources with limited near-surface expression, consistent with a structural framework that is not solely controlled by shallow surficial effects. We do not equate this continuation height with a specific source depth; depth attribution in this study relies on the independent Euler deconvolution solutions presented above [69]. Importantly, the spatial association between upward-continued magnetic features and known mineral occurrences remains evident. Gold deposits are commonly aligned with magnetic gradients and transition zones, whereas phosphate occurrences are generally associated with comparatively lower magnetic responses. The persistence of these relationships after upward continuation indicates that the mineralization pattern is linked not only to shallow heterogeneities but also to deeper magnetic structures that may have guided fluid flow and emplacement. Such behavior is typical in mineral prospectivity studies, where upward continuation is used to distinguish deep-seated geological controls from shallow noise and to improve the interpretation of regional mineralization patterns [64].

The qualitative interpretation of RTP and UC maps is often challenging and may lead to ambiguous conclusions. To overcome these limitations, the application of signal enhancement techniques is essential to improve image clarity and support more reliable geological interpretation. To precisely map the margins of both superficial and deep-seated magnetic anomalies, we processed the RTP and UC datasets using two cutting-edge edge-detection techniques, the Improved Logistic (IL) and the log-sigmoid function of the Horizontal Gradient (LSF) [8–10,52,66]. Their high-resolution response facilitates clear discrimination of anomalies associated with both high- and low-amplitude magnetic sources by enhancing subtle signal variations. In contrast, conventional RTP maps often fail to adequately resolve these differences (Figures 2b and 3).

Figure 3 presents the delineation of magnetic source boundaries as derived from the IL and LSF edge-detection filters. These advanced methods produce high-resolution and reliable outputs, supporting a more integrated and refined interpretation of the subsurface structural framework across the study area. A major advantage of these filtering methods is their capacity to sharpen anomaly peaks and better delineate source boundaries. The magnetic field is dominated mainly by positive anomalies, with the principal structural trends oriented N–S, NW–SE, and NE–SW, while subordinate E–W features are also present, as illustrated in Figure 3. When the filters are applied to the RTP and upward-continued data at 1 km and 2 km elevations (Figure 2), the number of identifiable anomalies decreases markedly. This reduction indicates that many of the resolved features are controlled by shallow magnetic sources. Figure 4 shows CET-derived structural maps obtained from processed magnetic data, including upward continuation to 1 and 2 km and subsequent application of the IL and LSF filters. Building on the patterns identified in Figure 3, these maps provide a more detailed structural framework and enable a more refined interpretation of the lineament network, thereby strengthening the geological basis for preliminary mineral exploration in the area.

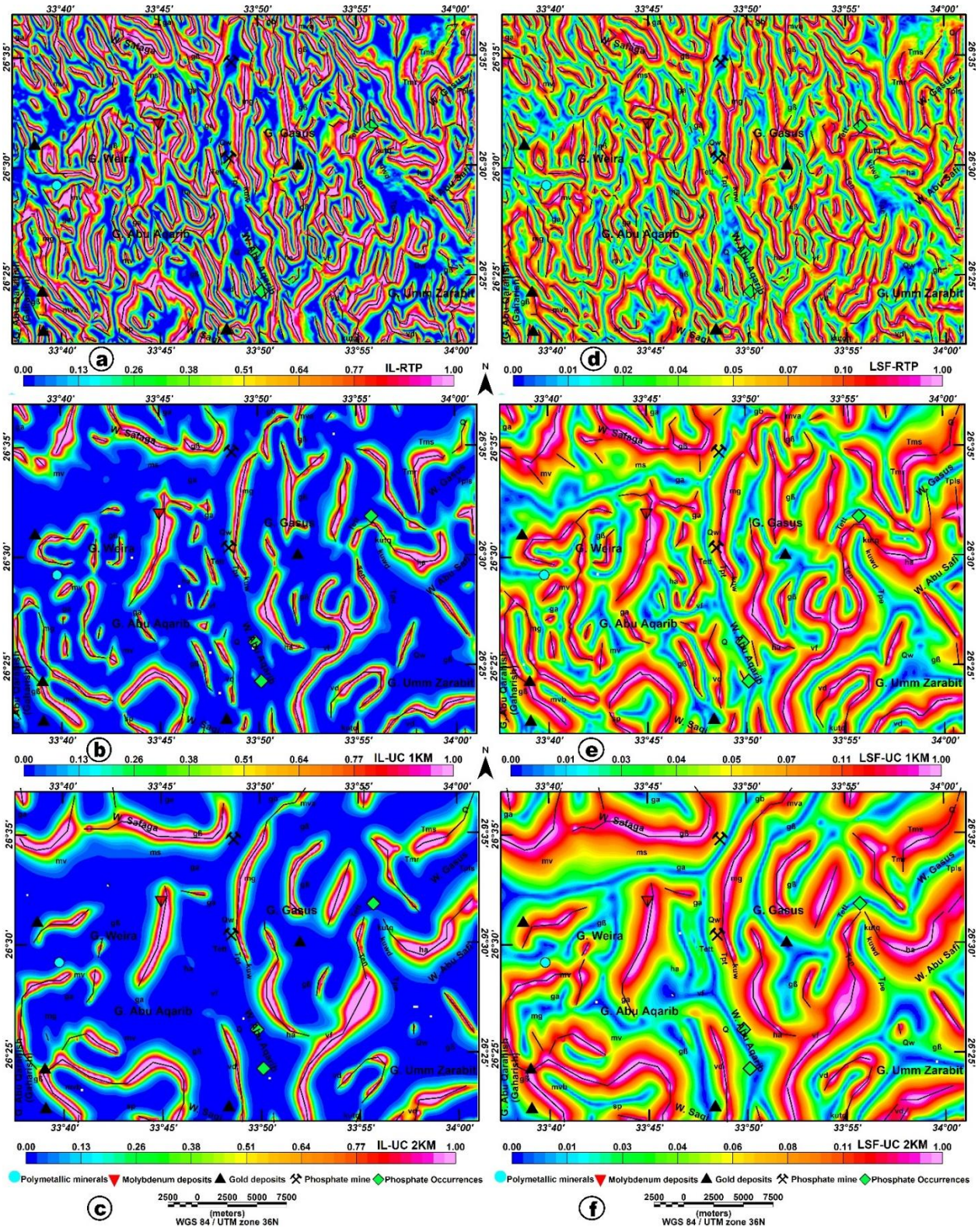


Figure 3. Magnetic edge-detection derivatives: (**a**–**c**) improved logistic (IL) outputs for RTP and upward-continuation heights of 1 km and 2 km; and (**d**–**f**) logsigm horizontal-gradient (LSF) outputs for the corresponding grids.

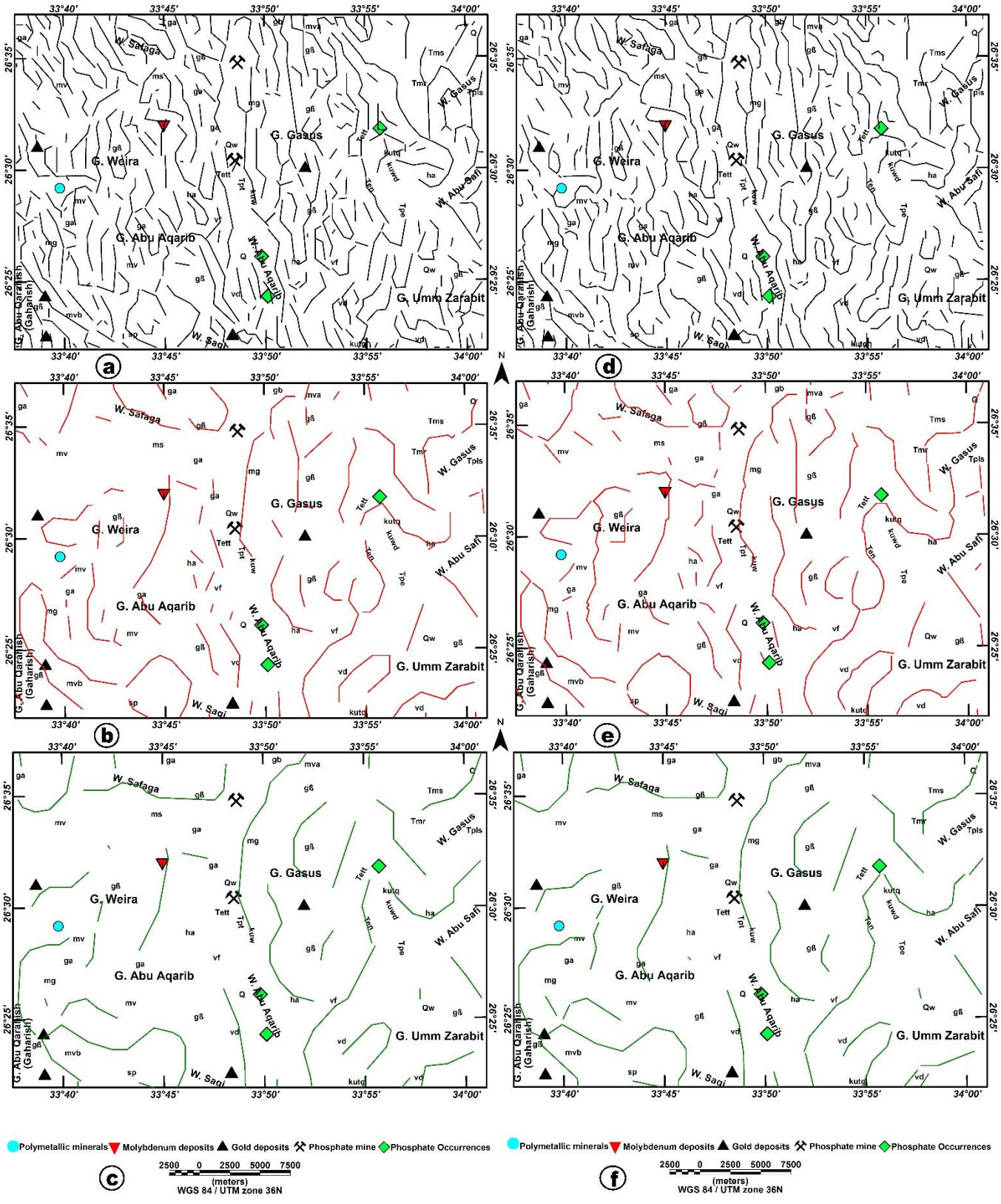


Figure 4. CET-GA structural maps of (**a**) IL-RTP; (**b**) IL-UC at 1 km; (**c**) IL-UC at 2 km; (**d**) LSF-RTP; (**e**) LSF-UC at 1 km; (**f**) LSF-UC at 2 km.

The rose diagrams (Figure 5) derived from the IL and LSF edge-detection products reveal a clear and persistent structural grain within the study area, with the dominant lineament populations concentrated mainly along N–S, NW–SE, and NE–SW orientations. This pattern is evident in the RTP-derived diagrams and remains recognizable after upward continuation, indicating that the mapped magnetic fabric reflects not only shallow

heterogeneities but also more persistent regional tectonic trends. Such directional clustering is consistent with the interpretation of lineament networks from aeromagnetic data, where edge-detection filters enhance linear discontinuities associated with faults, contacts, and shear zones.

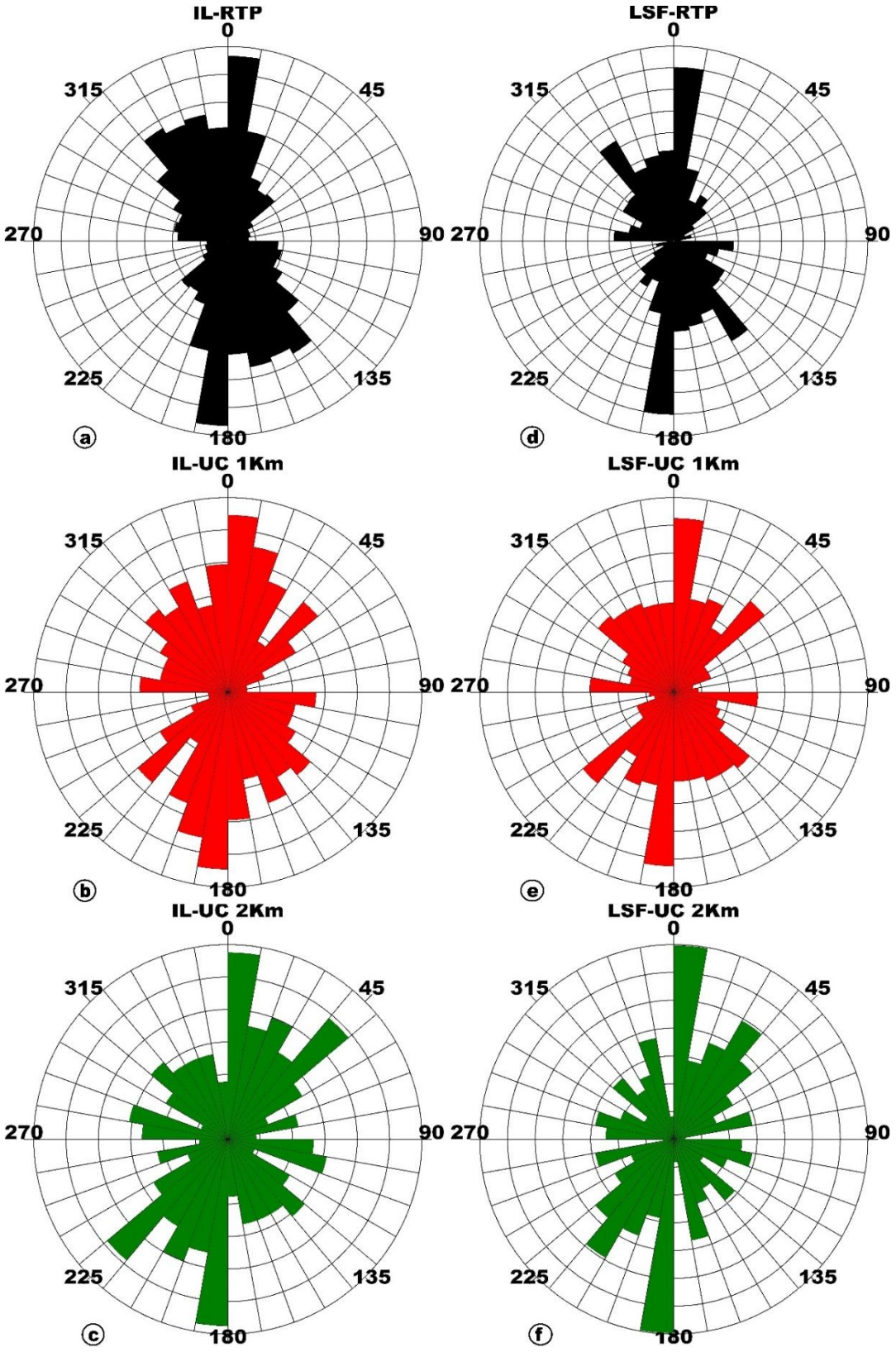


Figure 5. Rose diagrams derived from CET-GA structural maps of (**a**) IL-RTP; (**b**) IL-UC at 1 km; (**c**) IL-UC at 2 km; (**d**) LSF-RTP; (**e**) LSF-UC at 1 km; (**f**) LSF-UC at 2 km.

In the IL-RTP diagram (Figure 5a), the strongest peaks are centered close to the N–S axis, with subsidiary maxima in the NW–SE and NE–SW sectors. The corresponding LSF-RTP plot (Figure 5d) shows a broadly similar trend distribution, although the response is comparatively more focused, reflecting the selective enhancement of edges by the LSF filter (Figure 3d). The agreement between the two RTP-based rose diagrams suggests that the principal magnetic lineaments are stable features of the subsurface architecture rather than artifacts of a single processing method. This coherence supports the use of multiple derivative and edge-detection filters to improve confidence in structural interpretation [52,67]. After upward continuation to 1 km, the IL-UC and LSF-UC rose diagrams become less noisy and more regionally organized (Figure 5b,e). The reduction in the number of minor azimuthal peaks indicates that many short-wavelength lineaments are suppressed at this continuation height, leaving behind the more persistent and deeper structural elements. The dominant N–S and subordinate oblique trends remain evident, implying that these orientations correspond to deeper-seated faults or lithological boundaries with regional significance. The 1 km continuation, therefore, acts as an effective filter for distinguishing local disturbances from broader tectonic lineaments [67,70].

At 2 km of continuation, the rose diagrams exhibit a smoother directional distribution, with the N–S trend remaining the most prominent in both IL and LSF outputs (Figure 5c,f). The oblique NW–SE and NE–SW components are still present, but their relative contribution is reduced, reflecting the preferential attenuation of shallower structural effects. The persistence of the same principal orientations across both upward-continuation levels indicates that the study area is organized by a multiscale fault framework, in which major basement structures control the magnetic fabric at depth. This is a common outcome in regional magnetic interpretation, where upward continuation highlights the directional stability of deep structures and suppresses shallow lineament clustering.

The CET-GA mapping approach clearly delineates zones of structural complexity and prominent linear magnetic features across the study area (Figure 4). This interpretation is further supported by the structural lineament density map (Figure 6a), which reveals a dense network of magnetic contrasts interpreted as dykes, lithological boundaries, faults, and shear zones. These structures are predominantly oriented N–S, NW–SE, NE–SW, and E–W, indicating a well-developed and multi-directional tectonic fabric. This observation supports their interpretation as regionally important structural or lithological trends, but it does not independently determine their depth or continuity. The structural lineament density map (Figure 6a) clearly highlights zones of intense structural complexity and delineates major linear magnetic features across the study area. Lineament density analysis is a critical step in mineral prospectivity mapping, as regions with high fracture and fault densities often correspond to pathways of enhanced crustal permeability, which are essential for the migration and localization of hydrothermal fluids [71,72]. As shown in Figure 6a, lineament density varies significantly, ranging from 0 to 7.08 m/km^2. The spatial distribution of these lineaments reveals a highly compartmentalized structural framework. The highest density zones (indicated by red to orange colors, 4.86–7.08 m/km^2) form distinct curvilinear and linear corridors. These high-density corridors are primarily concentrated in the central and western sectors of the area, notably flanking Jabal Gasus, traversing near Jabal Weira, and trending along major wadi systems such as W. Safaga and W. Abu Aqarib. These zones of structural convergence are interpreted as major deformation zones, shear networks, or complex lithological contacts.

Conversely, areas of low lineament density (dark to light green, 0–2.36 m/km^2) are broadly distributed in the intervening regions, representing structurally intact or massive lithological blocks with minimal magnetic disruption. These lower-density zones likely correspond to the unfractured cores of intrusive bodies [73]. A critical observation from the density map is the strong spatial correlation between zones of high lineament density

and the known distribution of mineral occurrences. Gold, molybdenum, and polymetallic occurrences are located within or at the margins of the high-density corridors (4.86–7.08 m/km^2). Phosphate occurrences are located in regions of moderate to low lineament density, at Wadi Abu Aqarib, near Wadi Gasus, and Wadi Abu Safi. This relationship strongly supports a structurally controlled epigenetic model of mineralization in the region, in which regional faulting and shearing provided the plumbing systems for ascending ore-bearing fluids [74].

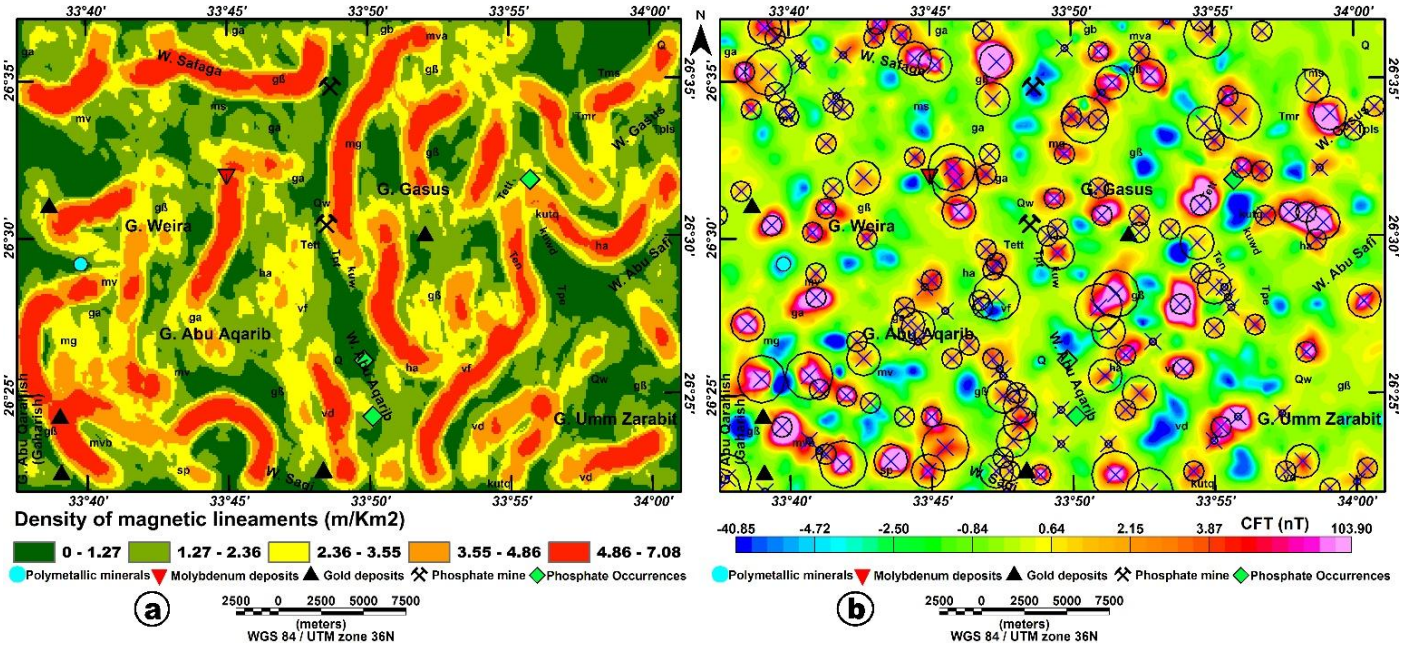


Figure 6. (**a**) Magnetic lineament density map, (**b**) circular feature transform (CFT) map.

In a complementary analysis, a set of CET-PA algorithms was applied to the RTP magnetic data from the study area to improve the detection of circular and semicircular anomalies commonly associated with porphyry-type intrusions. Such features often mark hydrothermally altered zones that may host significant mineralization (Figure 6b). The delineated porphyry bodies show a strong spatial association with structurally complex domains and frequently follow trends comparable to those of mapped lineaments. CET-PA delineates several circular to semicircular magnetic features, including clusters around Jabal Gasus, Jabal Weira, Jabal Abu Aqarib, and W. Abu Safi (Figure 6b). They vary in magnetic contrast and coincide locally with mapped lineaments and magnetic gradients. Notable clusters occur within the structurally complex corridors around G. Gasus, G. Weira, G. Abu Aqarib, and W. Abu Safi, where they coincide with major lineament trends and strong magnetic gradients (Figure 6b). The circular to semicircular geometry of these features is consistent with intrusive bodies emplaced in a deformational framework and is commonly regarded as a diagnostic magnetic signature of porphyry systems [56,75].

The detected porphyry-related anomalies vary in size and magnetic intensity, with many appearing as high-contrast ring-like patterns. Their spatial clustering around areas of structural intersections suggests that emplacement was strongly controlled by pre-existing fault and fracture systems. This structural association is significant because porphyry intrusions are frequently emplaced along zones of enhanced crustal permeability and are closely linked to hydrothermal alteration and fluid focusing [56,75,76]. A notable outcome of the CET-PA processing is the clear correspondence between the mapped circular anomalies and known mineral occurrences. Several of the porphyry-like bodies occur near gold, molybdenum, and polymetallic units, indicating that these structures may have played a role in channeling mineralizing fluids or localizing alteration halos.

Although not every anomaly necessarily represents a mineralized intrusion, the repeated spatial association between the CET-PA signatures and prospective areas increases the exploration significance of the detected features. Such responses are widely interpreted as favorable targets in magnetic studies because porphyry intrusions can act as both heat sources and structural traps for hydrothermal systems [75,76].

Integrating precise depth estimation with edge-enhancement techniques improves geological interpretation by revealing the spatial distribution and geometry of subsurface structures in greater detail [77,78]. The EUD method is highly effective at isolating subsurface structural boundaries by relating the magnetic field and its gradients to the location and depth of the source using a designated structural index (SI) [78]. Euler solutions were calculated for three assumed structural indices: SI = 0.0 (Figure 7a), 0.5 (Figure 7b), and 1.0 (Figure 7c). These values represent alternative idealized source geometries and were used to evaluate the sensitivity of solution locations and depths to source-model assumptions. Therefore, the three solution maps should not be interpreted as independent confirmation of discrete contact, dyke, and fault levels, nor as evidence for a uniquely resolved vertically stratified crustal architecture. Their primary value is to identify zones where solution clusters recur spatially across plausible geometrical assumptions.

For geological contacts (SI = 0), the solutions (Figure 7a) are dominated by shallow-depth estimates, with the vast majority of points located at depths less than 500 m (black dots). These shallow solutions tightly trace the major lithological boundaries and delineate the intricate network of mapped outcropping and near-surface contacts. This agreement supports a contact-related interpretation for some anomalies, but the estimated depths remain conditional on the SI = 0.0 source model and should not be regarded as direct measurements of contact depth. The histogram confirms this strong shallow bias, indicating that the primary lithological contrasts in the region are exposed or lie just beneath a thin cover sequence.

When the structural index is increased to SI = 0.5 to target dykes (Figure 7b), the depth distribution shifts significantly deeper. While shallow sources (<500 m) remain abundant, there is a pronounced increase in solutions within the 500–1000 m range (blue dots), particularly along the dominant N–S and NW–SE trends. Some solutions also extend into the 1000–1500 m range (green dots). The fault model (SI = 1, Figure 7c) displays the most depth-extensive distribution of Euler solutions. The map reveals continuous linear features that extend from the near-surface (<500 m) down to depths exceeding 1500 m (green and yellow dots), with isolated solutions reaching beyond 2000 m (red dots) in the northeastern sector near W. Gasus. The corresponding histogram illustrates a broad, bell-shaped distribution peaking between 500 m and 1000 m.

The three Euler models identify several areas where solution clusters, magnetic gradients, mapped lineaments, lithological contacts, and known mineral occurrences coincide. These spatial associations support the interpretation that structural and lithological discontinuities may have influenced permeability and localized hydrothermal alteration and mineralization. However, overlap between SI = 0.5 and SI = 1.0 solution clusters is not treated as independent confirmation of separate dyke and fault levels, because both solution sets are derived from the same magnetic field under different assumed source geometries. Consequently, the intersection of shallow contacts with deeper fracture networks identified by the EUD method constitutes a highly prospective setting for epigenetic mineralization.

The spatial distributions of potassium (%K), equivalent thorium (eTh), and equivalent uranium (eU) show pronounced regional variability that correlates strongly with the mapped geological units and structural framework of the study area (Figure 8). The radiometric maps exhibit a clear split division, with generally low radioelement concentrations in the western sector and significantly elevated responses in the central and eastern

domains. By correlating these patterns with the geological map, the low eTh, eU, and %K values in the west (around Jabal Weira and Jabal Abu Aqarib) coincide predominantly with Precambrian metavolcanics (mv), metagabbro to metadiorite (mg), and ophiolitic serpentinites (sp). These mafic-to-intermediate units inherently have low primary abundances of radioactive elements, and their subdued radiometric signatures are consistent with their mapped distribution.

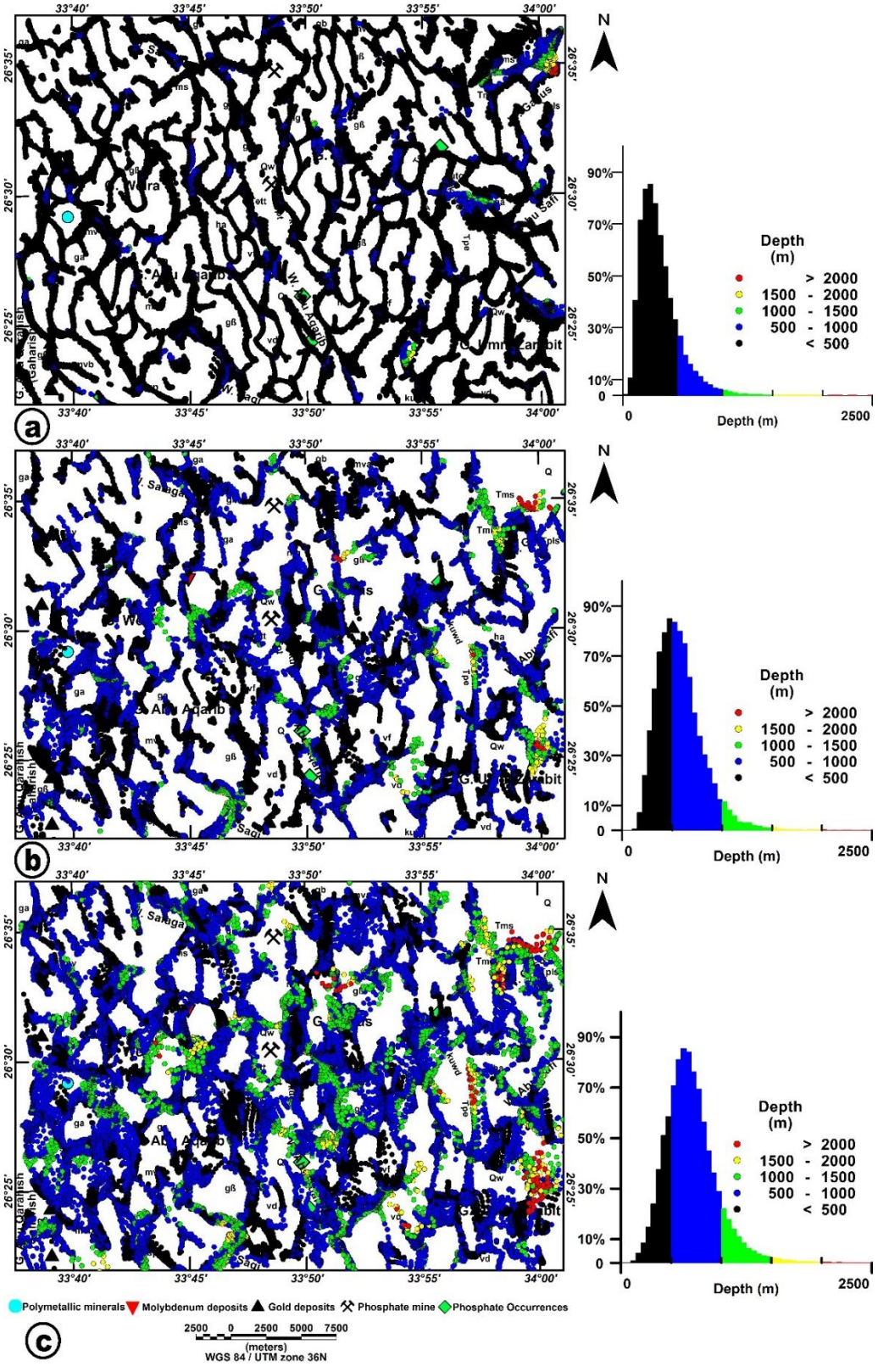


Figure 7. EUD depth solutions (**a**) SI = 0.0, (**b**) SI = 0.5, (**c**) SI = 1.0 of the study area.

https://doi.org/10.3390/min16111099

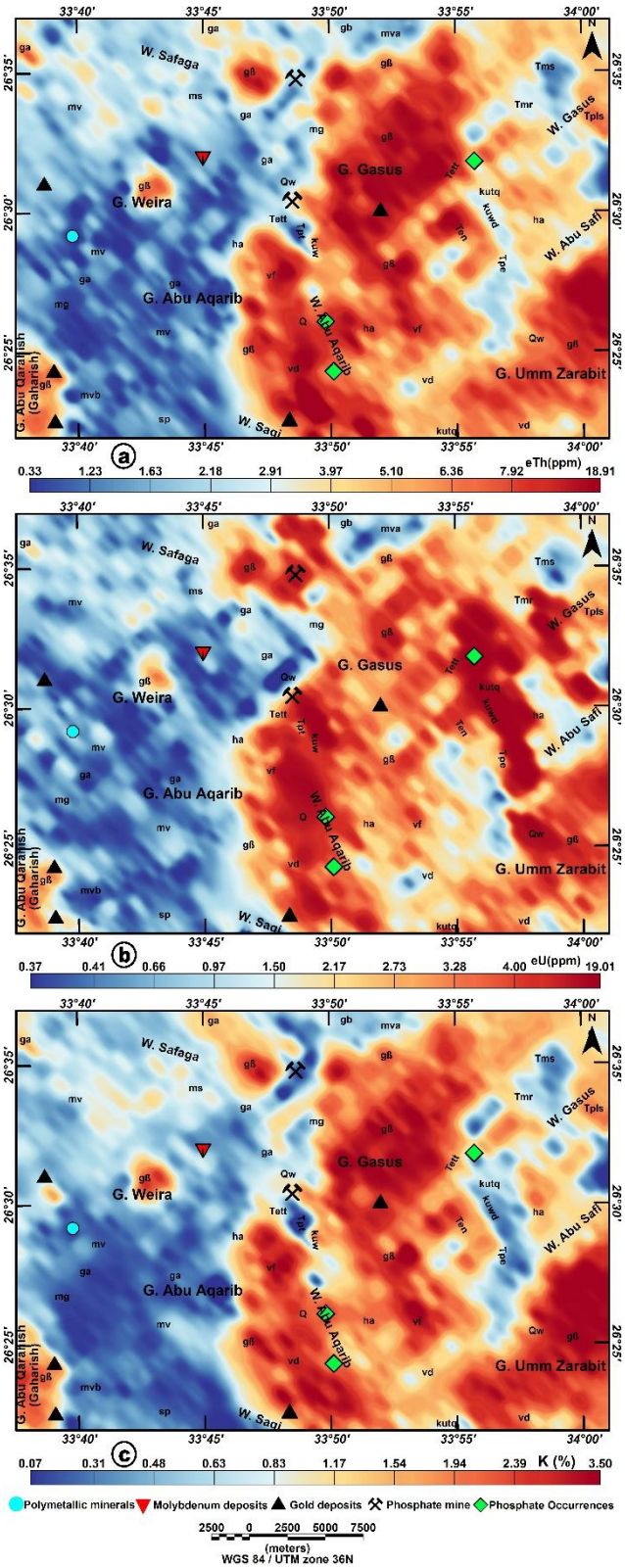


Figure 8. Radiometric maps of the study area: (**a**) %K, (**b**) eTh, and (**c**) eU.

In contrast, the prominent high-radiometric anomalies in the central and eastern sectors correlate with specific felsic intrusions and younger sedimentary units. The highest %K and eTh responses are distinctly associated with the Calc-alkaline granite (Younger Granite, gβ) complexes exposed around Jabal Gasus and Jabal Umm Zarabit, as well as the Dokhan volcanics (vd) and post-Hammamat felsites (vf). The strong potassium and

thorium signatures are diagnostic of the evolved, potassic nature of these felsic rocks, reflecting the abundance of primary K-feldspar and accessory minerals such as zircon and monazite [79]. The equivalent uranium (eU) distribution is more localized and structurally controlled. While elevated eU generally overlaps with the Younger Granites and felsic volcanics, anomalous, patchy eU concentrations also occur along major structural contacts and within the Cretaceous–Tertiary sedimentary successions in the eastern wadi systems (e.g., W. Gasus and W. Abu Safi). The Duwi Formation (kuw), which hosts the known phosphate beds and mines, exhibits distinct but highly localized uranium signatures, a common characteristic of uranium substitution into the carbonate-fluorapatite lattice of marine phosphorites [80]. Furthermore, some mapped fault corridors, particularly those trending N–S and NW–SE across metavolcanic and granitic domains, coincide with elevated potassium and uranium responses. These spatial associations identify sites for follow-up, but may also reflect lithological contrasts along the corridors. Possible radioelement redistribution or potassic alteration should therefore be assessed using independent evidence of fluid–rock interaction rather than inferred directly from the radiometric high [81]. Anomalous K and eU values accompany N-S and NW-SE fault corridors that cut the metavolcanic and granitic domains. Gold and polymetallic occurrences are located mainly in transition zones between the low-radioactivity metavolcanic/ophiolitic rocks and the high-radioactivity granites, where radiometric and magnetic gradients are sharp.

The spatial distributions of the F-parameter [82] and Kd values [83] show strong lateral variation across the study area (Figure 9). When interpreted together with the geological map, both parameters clearly discriminate between mafic–ultramafic, metavolcanic, felsic, and sedimentary domains. These are radiometric geochemical products and are not measures of magnetization, magnetic gradients, magnetic-source geometry, or structural edge sharpness. Structural relationships are evaluated separately using geological mapping and magnetic derivatives.

The F-parameter map (Figure 9a) displays broad high-value zones in the central to eastern parts of the area, especially around Jabal Gasus, Jabal Umm Zarabit, and the W. Abu Safi corridor. These zones overlap mainly with calc-alkaline granite and felsic volcanic rocks on the geological map, consistent with variations in K abundance and the eU/eTh ratio. High F-parameter values may occur in felsic igneous units or in hydrothermally modified rocks, but do not distinguish these alternatives on their own [67]. High F values identify radiometric geochemical contrasts rather than magnetic-source configurations or magnetic gradients. The central–eastern high-F domain corresponds principally to K- and eU-enriched felsic and sedimentary units, whereas lower F values in the western sector correspond to relatively K-, eU-, and eTh-poor metavolcanic, metagabbroic, and ophiolitic rocks. Thus, the observed separation is interpreted primarily as a lithological radiometric contrast. Any alteration-related interpretation is restricted to locations where other independent evidence supports fluid–rock interaction. The Kd map (Figure 9b) represents the residual between observed K and the K value predicted from the local K–eTh background relationship. Negative Kd values indicate K depletion relative to the selected thorium-controlled background; positive Kd values indicate K enrichment relative to that background. Low or negative Kd values are not evidence of hydrothermal enrichment. They may reflect K-poor primary lithologies, K loss during alteration, weathering, regolith development, mixed lithologies, or limitations of the local regression model. Positive Kd values may be compatible with K addition, including potassic alteration, but they may also reflect K-rich primary lithologies; therefore, neither sign is diagnostic of hydrothermal alteration in isolation [28]. Positive Kd values are concentrated in parts of the central–eastern domain, where they overlap with felsic intrusive and volcanic units. This distribution may reflect primary K-rich lithologies, such as K-feldspar-bearing granites and fel-

sic volcanic rocks, and/or localized K addition. The association of some positive-Kd anomalies with mapped structures and mineral occurrences makes these sites appropriate targets for field verification, but it does not establish hydrothermal alteration.

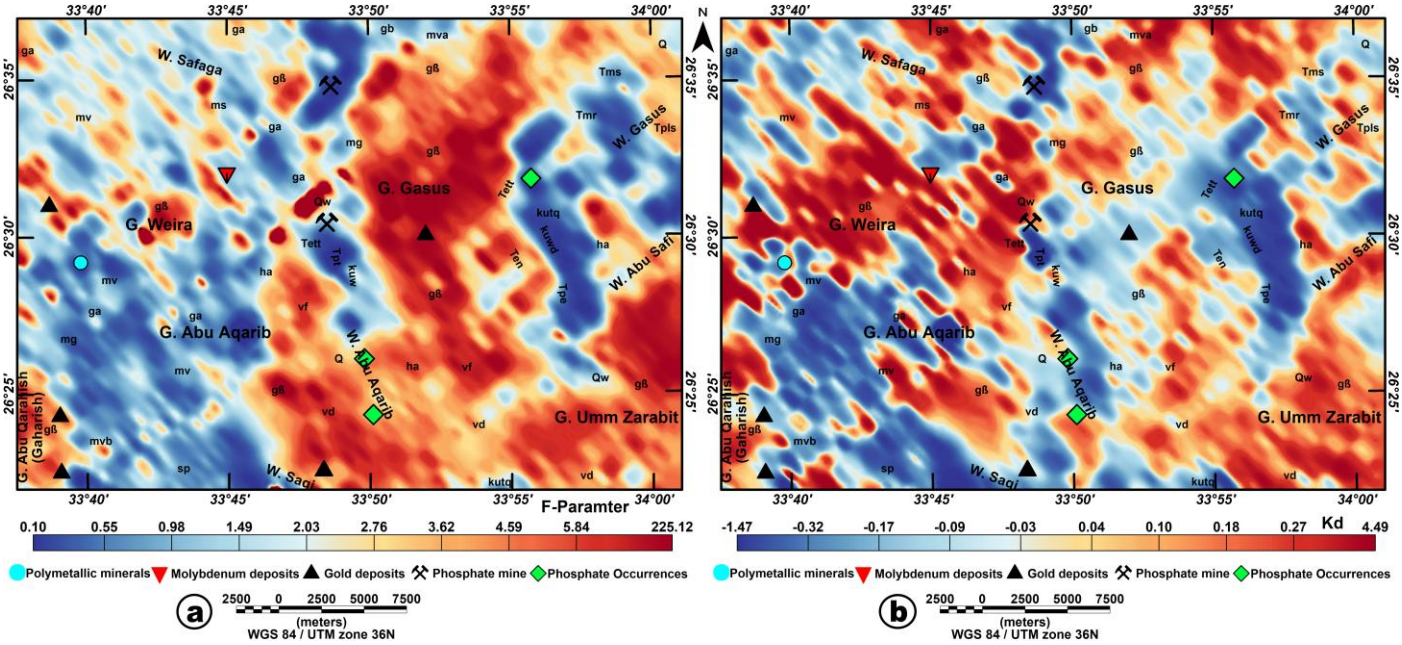


Figure 9. (**a**) F-parameter map, (**b**) potassium deviation (Kd) map. Positive Kd denotes relative K enrichment and negative Kd denotes relative K depletion with respect to that statistical background. Neither map independently demonstrates hydrothermal alteration.

The ternary map of radioelements and the K-, eTh-, and eU-composite maps (Figure 10) reveal a pronounced lithological radiometric contrast across the study area. Comparison with the geological map indicates generally low radioelement responses over the western mafic–ultramafic basement and elevated responses over the central and eastern felsic and sedimentary units. These products display the spatial distribution and relative contributions of K, eTh, and eU and support comparison with mapped geological units [28]. The observed regional patterns are interpreted primarily in terms of lithological composition. Possible hydrothermal redistribution is considered a local hypothesis requiring independent supporting evidence, rather than an established explanation for the composite signatures. Figure 10a summarizes the relative radioelement responses; its colors are not classifications of alteration intensity.

The ternary map (Figure 10a) shows potassium-rich signatures in the central and eastern sectors, broadly corresponding to calc-alkaline granite, post-Hammamat felsite, Dokhan volcanics, and sedimentary units. The western sector is dominated by lower radiometric responses over metavolcanics, metagabbro to metadiorite, and ophiolitic serpentinite. The K-composite map (Figure 10b) highlights elevated potassium responses around Jabal Gasus, Jabal Umm Zarabit, and the W. Abu Safi corridor. Their overlap with felsic intrusive and volcanic units supports a primary lithological explanation involving K-bearing minerals. Some high-K responses also coincide with mapped structural lineaments, making these locations useful for targeted follow-up. This spatial association alone does not distinguish primary K enrichment from hydrothermal K addition and does not establish potassic alteration or sericitization. An alteration interpretation would require independent evidence of fluid–rock interaction at the corresponding sites.

The eTh-composite map (Figure 10c) shows elevated responses mainly in central and eastern domains, with broader patterns than those in the K map. Their correspondence with granite, felsite, and evolved volcanic units is interpreted primarily as a lithological

signal associated with the distribution of eTh-bearing accessory minerals. Lower eTh responses over the western mafic–ultramafic domain are consistent with the contrasting composition of these units. High eTh values are not treated as evidence of hydrothermal alteration. The eU-composite map (Figure 10d) displays more localized elevated responses in the central and eastern sectors, some near-lithological contacts, mapped faults, and wadi corridors. Responses near phosphatic and sedimentary units are evaluated first in their stratigraphic and lithological context. Secondary uranium redistribution remains a possible explanation for some local anomalies, but the mapped patterns alone do not establish its mechanism or a hydrothermal origin. The western basement domain generally shows lower eU responses, consistent with its predominantly mafic–ultramafic composition.

Collectively, the ternary and composite radiometric maps emphasize lithological variation, with stronger responses over central–eastern felsic and sedimentary units and lower responses over the western mafic–ultramafic western domain. Where radiometric contrasts coincide with mapped structures and documented mineral occurrences, they provide complementary criteria for regional target prioritization. These coincidences identify sites for geological verification rather than confirmed alteration corridors or mineralized intrusive centers. Hydrothermal alteration remains a conditional interpretation to be evaluated using independent geological, mineralogical, and geochemical evidence.

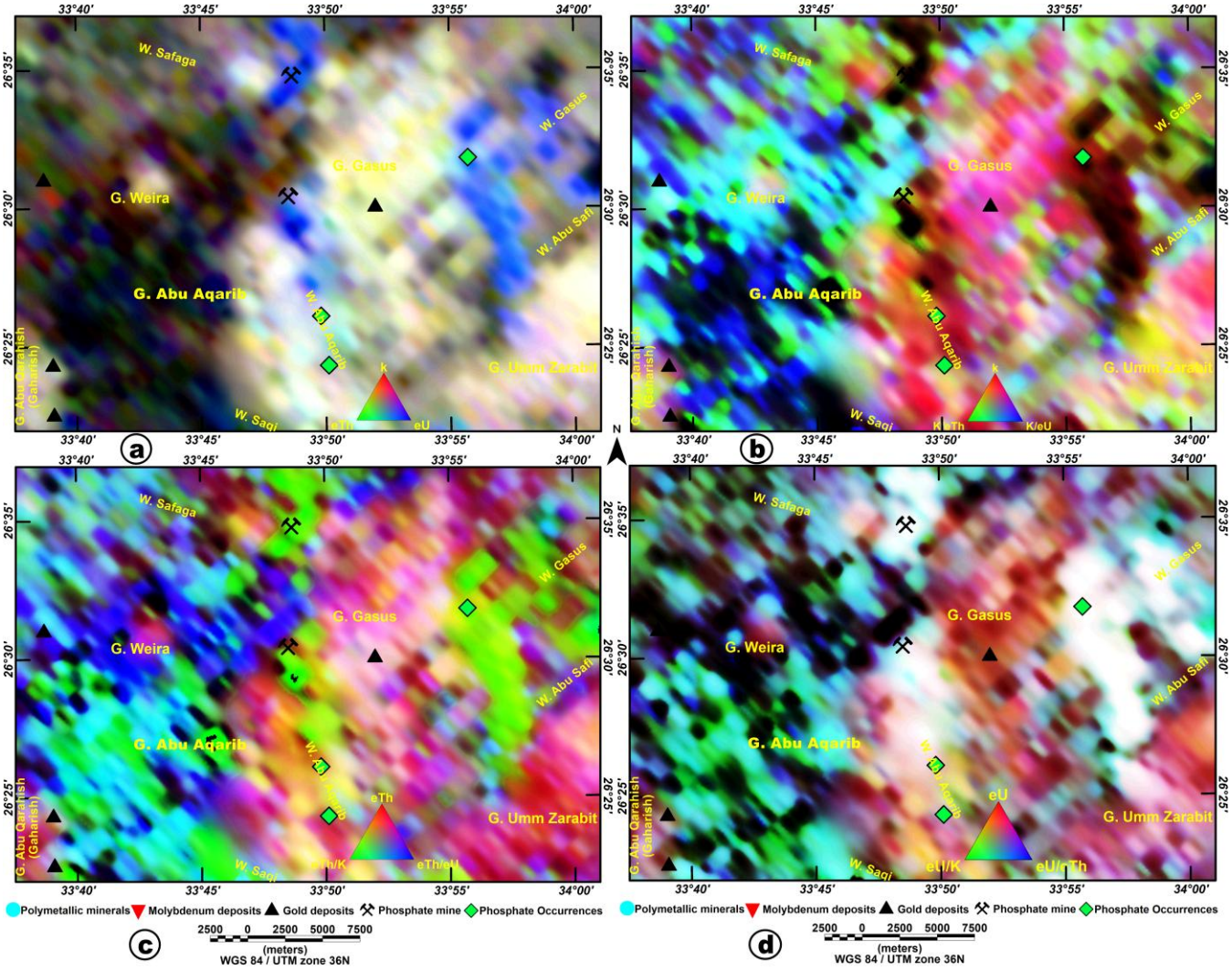


Figure 10. Radiometric products of the study area: (**a**) radioelements ternary map, (**b**) K-composite map, (**c**) eTh-composite map, and (**d**) eU-composite map.

The fuzzy prospectivity map (Figure 11) shows spatially variable scores. At the adopted class thresholds, the highly favorable class occupies 62.53% of the area and therefore represents a broad screening domain rather than a narrowly delineated set of exploration targets. The high fuzzy values are concentrated mainly in the central and eastern sectors, particularly around Jabal Gasus, W. Abu Safi, Jabal Umm Zarabit, and parts of W. Abu Aqarib, where they coincide with mapped structural intersections, intrusive contacts, and radiometric-magnetic anomalies.

The spatial pattern suggests that mineral prospectivity reflects the combined influence of lithology, deformation, and hydrothermal alteration, consistent with fuzzy-logic exploration models [62,84]. High-prospectivity zones concentrate along the margins of calc-alkaline granite, post-Hammamat felsite, and Dokhan volcanics, where fracturing and alteration may promote fluid flow and mineral precipitation. Gold, molybdenum, and polymetallic occurrences fall within or close to high-score areas, supporting the model's geological relevance. Phosphate occurrences are not part of the evaluation. Near Jabal Weira, Jabal Gasus, and W. Abu Aqarib, anomalies coincide with major lineaments and intrusive contacts, suggesting structural control rather than lithological enrichment alone. The western and southwestern sectors have low scores. Similar spatial correspondence between fuzzy prospectivity and mineralized corridors has been reported in other knowledge-driven targeting studies, confirming the utility of fuzzy integration for combining multi-source geoscientific evidence [74,85]. In contrast, the western and southwestern sectors, dominated by metavolcanics, metagabbroic rocks, and ophiolitic serpentinite, are generally assigned low fuzzy values. These areas are comparatively less prospective because they lack the strong radiometric enrichment, intrusive association, and structural complexity observed in the central-eastern part of the map. Their subdued response suggests either limited hydrothermal alteration or lithologies less favorable for the development of mineralized systems. The spatial contrast between high- and low-score domains therefore reflects a clear geological zoning that is consistent with the mapped bedrock framework.

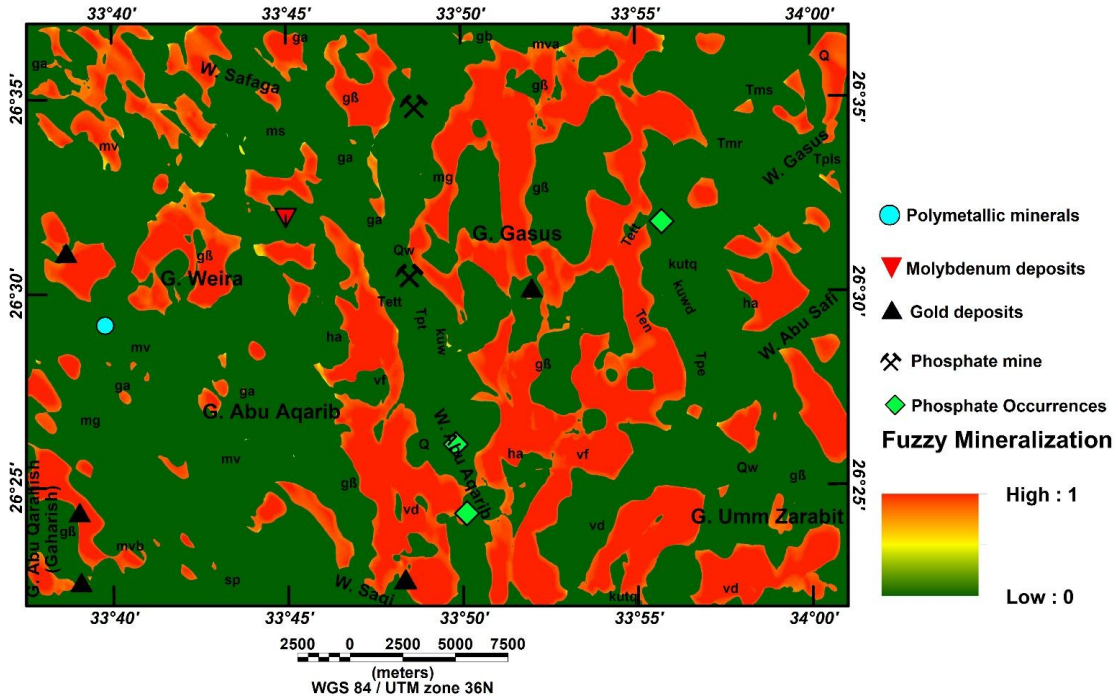


Figure 11. Fuzzy overlay mineral prospectivity of the Jabal Gasus area; black triangles = gold, red inverted triangles = molybdenum, cyan circle = polymetallic (Cu-Pb-Zn), green diamonds and crossed hammers = phosphate occurrences and mines.

The areas and occurrence statistics of the favorability classes are given in Table 1. The highly favorable class covers 729.67 km² (62.53% of the study area) and contains 5 of the 7 hydrothermal occurrences (71.43% of the hydrothermal occurrences). The moderately favorable class covers 12.94 km² (1.10%) and contains none. The poorly favorable class covers 424.24 km² (36.35%) and contains 2 occurrences (28.57%). The occurrence density is 0.69 per 100 km² in the highly favorable class and 0.47 per 100 km² in the poorly favorable class, and the ratios of occurrence share to area share are 1.14 and 0.79, respectively. Phosphate occurrences are excluded from these statistics. The highly favorable class shows modest enrichment of known occurrences (ratio 1.14 vs. 0.79). Given its broad extent and two hydrothermal occurrences in the poorly favorable class, the map is suitable only for regional prioritization. These descriptive statistics do not establish predictive performance for undiscovered deposits. Gamma was selected by re-running the overlay for gamma = 0.70, 0.80, and 0.90 with the evidence layers, membership functions, and equal weights unchanged. The AUC increased from 0.685 (gamma = 0.70) to 0.707 (gamma = 0.80) and 0.733 (gamma = 0.90) (Table 2; Figure 12), and gamma = 0.90 was adopted. Because the same seven occurrences guided gamma selection and model assessment, the AUC values reflect internal success-rate performance rather than independent validation. With no independent test data or spatial cross-validation and a small sample, the robustness of the assessment is limited. Independent testing with additional occurrences is needed to confirm predictive capability and targeting effectiveness.

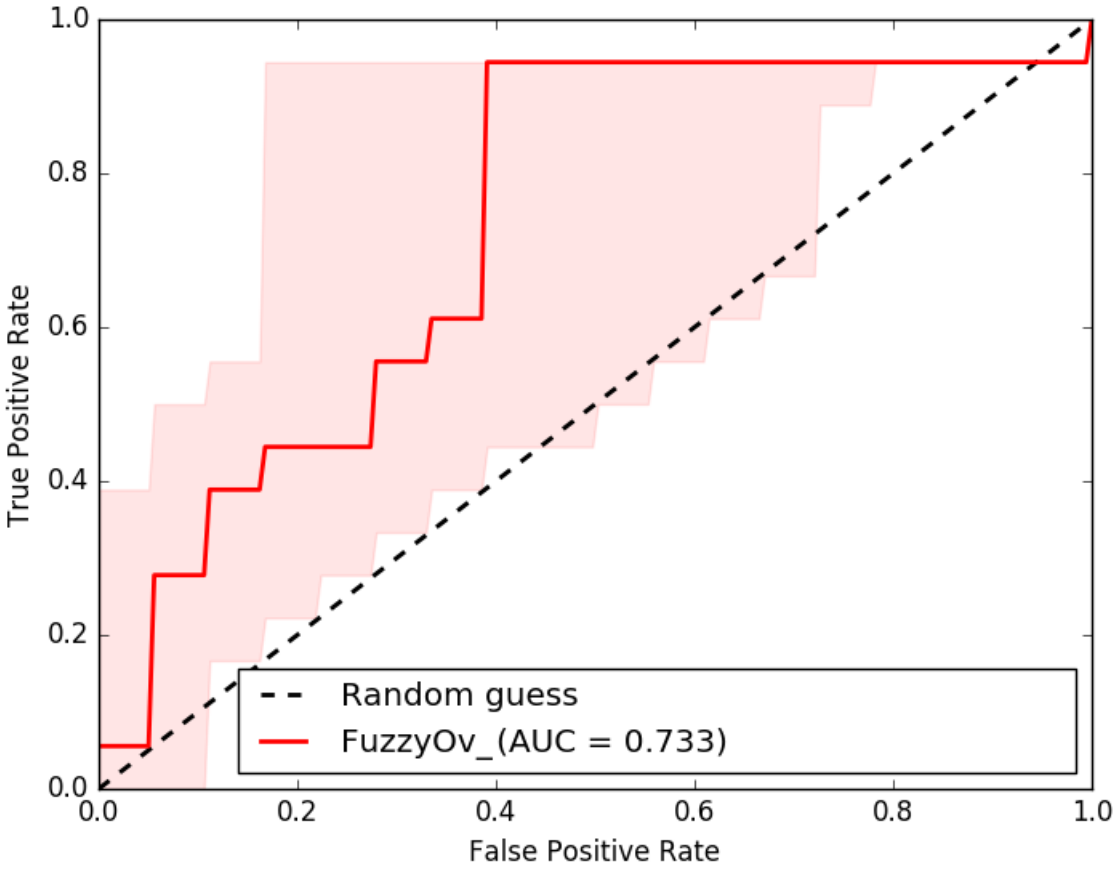


Figure 12. ROC curve (AUC = 0.733) of the fuzzy overlay prospectivity model (gamma = 0.90), based on seven hydrothermal occurrences; phosphate occurrences are excluded.

Table 1. Distribution of mineralization potential in the study area.

Favorability Class	Fuzzy Score Range	Area (km²)	Area (%)	Number of Hydrothermal Occurrences	Occurrences (%)	Occurrences per 100 km²	Occurrence Share/Area Share
Highly favorable	>[0.6]	729.67	62.53%	5	71.43%	0.69	1.14
Moderately favorable	[0.4]–[0.6]	12.94	1.10%	-	-	0.00	0.00
Poorly favorable	<[0.4]	424.24	36.35%	2	28.57%	0.47	0.79
Total	-	1166.85	100%	7	100%	0.60	1.00

Table 2. Sensitivity of fuzzy model performance to gamma.

Gamma (γ)	AUC	Change in AUC Relative to γ = 0.90	Evidence Layers	Membership Functions	Layer Weights
0.70	0.685	−0.048	Unchanged	Unchanged	Unchanged (equal)
0.80	0.707	−0.026	Unchanged	Unchanged	Unchanged (equal)
0.90 (selected)	0.733	0.000	Unchanged	Unchanged	Unchanged (equal)

5. Discussion

The accelerated global transition toward renewable energy technologies has heightened demand for critical mineral deposits, placing the Egyptian–Nubian Shield (ENS) and similar Precambrian terranes at the forefront of exploration frontiers. Yet conventional exploration models, reliant on comprehensive drilling and ground-based surveys, entail high economic and environmental costs. The incorporated geophysical framing applied in the Jabal Gasus region reveals that systematic interpretation of aeromagnetic and aeroradiometric data can jointly illustrate the structural framework of mineral systems and provide a potential pathway for unearthing. By synthesizing magnetic and radiometric data with advanced enhancement strategies, including IL [23] and LSF edge detectors [53], CET-GA [27,33] and CET-PA [56], EUD [54], and fuzzy logic prospectivity modeling [60–62], this investigation demonstrates a logical mineral system model that relates the Neoproterozoic tectonic evolution of the Central ENS to the locative distribution of polymetallic mineralization. Analysis of aeromagnetic data reveals a structurally complicated but systematically organized pattern that documents the polyphase tectonic development of the Jabal Gasus region. The RTP map (Figure 2b) shows pronounced spatial variety, with high-value anomalies concentrated around east Jabal Abu Qarahish, Wadi Gasus, and Jabal Gasus. At the same time, low-amplitude parts characterize the southeastern and western sectors around Jabal Umm Zarabit and Jabal Weira. This magnetic contrast reflects fundamental structural and lithological differences that are paramount to understanding mineralization regimes. These anomalies may reflect magnetized felsic- to intermediate-composition bodies. Their relationship to mapped contacts and shear zones is compatible with structural influence on emplacement but does not uniquely establish source lithology or emplacement history [32,65]. Low magnetic responses may also be compatible with local demagnetization, although a hydrothermal explanation requires evidence beyond anomaly amplitude.

Applying IL and LSF techniques to RTP and UC data (Figure 3) provides an unprecedented explanation of structural lineaments at various depths. Lineament analysis (Figure 4) and rose diagram (Figure 5) reveal a structural grain controlled by N-S, NW, and NE directions, with subordinate E-W components. Critically, UC to 2 km suppresses short-wavelength components and underscores the persistence of the N-S direction, demonstrating that these systems are deeply rooted and characterize crustal-scale discontinuities that have often been reactivated. This observation aligns with the conclusions of Eldosouky et al. [86], Abd El-Wahed et al. [87], and Abd El-Wahed and Eldosouky [88],

who demonstrated a comparable structural framework in the adjoining Safaga–Semna shear-belt (SSSB), and with those of Zaki et al. [5], who recognized NW as the prevailing deep-seated direction in the Gasus region.

The value of this structural analysis lies in its role as a plumbing pattern for mineralized fluids. The lineament density map (Figure 6a), with values varying from 0 to 7.08 m/km^2, emphasizes distinct linear and curvilinear corridors of highest structural intricacy in the western and central sectors, specifically the zones where known mineralized occurrences are concentrated. Molybdenum occurrences, Gold (black triangles) deposits, and polymetallic spots are almost exclusively located within or at the margins of these high-density passageways. This spatial correlation is not a coincidence but reflects the essential role of crustal permeability in ore deposition and fluid migration. As illustrated by McCuaig and Hronsky [74] and Groves et al. [71], orogenic gold deposits are localized in distinctive structural environments that provide both fluid pathways (shear zones and major faults) and depositional sites (rheological contrasts, fault intersections). The CET-GA lineament maps (Figure 4) further refine this understanding by delineating regions of structural complexity that conform to zones of intense shearing and fracturing. The consistency between the IL and LSF outcomes, when applied to both RTP and UC data, demonstrates that the mapped structural features are strong features of the deep architecture rather than artifacts of a single enhancement filter.

Euler deconvolution contributes a set of model-dependent source-location estimates that complement the magnetic gradient, CET, and geological interpretations. The SI = 0.0 scenario yields predominantly shallow estimates that broadly coincide with some mapped lithological boundaries. This correspondence is consistent with contact-like sources, but it does not uniquely distinguish shallow contacts from other geometries capable of producing similar magnetic gradients. These contacts, mostly between granitic intrusions and metavolcanic/ophiolitic successions, describe rheological contrasts that may have concentrated fluid flow but are themselves not the prior control on mineralization. Instead, they act as local traps where fluids ascending along deeper conduits encounter favorable physical and chemical conditions for ore deposition.

The spatial coincidence of known polymetallic and gold occurrences with zones where SI = 1.0 solutions cluster at depth is consistent with these structures having acted as upper-crustal conduits for mineralizing fluids. Because the Euler solutions in this study are confined to depths of less than ~2 km, they constrain only the shallow-to-intermediate expression of the fault network and do not provide evidence for fluid sourcing from the deep crust or mantle; any such origin would require independent geochemical, isotopic, or deep-geophysical (e.g., magnetotelluric or seismic) constraints not available. This agrees with the determinations of Ghoneim et al. [32], who recorded shallow EUD solutions (0.1–0.2 km) at the Abu-Marawat gold mine, and with the deeper ones (0.2–1.1 km) determined by Zaki et al. [5] for the sedimentary basins in the Gasus region. The SI = 0.5 solutions provide intermediate depths (0.5–1.5 km), mainly along the prevalent N-S and NW-SE directions. These estimates may be compatible with intrusive or structural sources along the dominant trends, but the inferred geometry and depth remain conditional on the Euler assumptions and do not independently establish a vertically connected fluid pathway [63,78]. These characteristics likely describe intrusive systems that exploit pre-existing fractures and may have provided secondary fluid paths. The existence of vertically comprehensive dyke networks is particularly influential for porphyry-style mineralization, as reported by the CET-PA (Figure 6b), which recognizes circular to semicircular anomalies around W. Abu Safi, Jabal Gasus, Jabal Abu Aqarib, and Jabal Weira. The emplacement of these intrusions presumably generated fracture systems facilitating localized alteration and hydrothermal fluid flow, a common diagnostic characteristic of porphyry networks [8,56,76,89]. The integration of UC at 1–2 km (Figure 2c,d) with EUD provides a

robust framework that was lacking for the Jabal Gasus region. The current investigation indicates that the depth to basement in areas with sedimentary cover ranges from 0.15 to 0.75 km, consistent with the 2D modeling results of [5], while providing adequate spatial resolution of the fault systems that control potential mineralization pathways and basin geometry.

The radiometric data provide crucial lithological radiometric contrast that complements the structural system emanated from magnetic data [90]. The spatial distribution of K, eU, and eTh (Figure 8) indicates a noticeable bipartite pattern: raised responses in the eastern and central domains (associated with post-Hammamat felsites, Dokhan volcanics, and calc-alkaline granite) and low concentrations in the western part (overlapping with ophiolitic serpentinites, metagabbro, and metavolcanics). This pattern agrees with the determinations of El Qassas et al. [45], who demonstrated the highest radiometric values over the Duwi Formation and younger granites in the neighboring Wadi Queih-Wadi Safaga region.

The radiometric derivatives complement lithological mapping by highlighting contrasts for further assessment. The F-parameter map (Figure 9a) shows broad high-value zones around W. Abu Safi, Jabal Umm Zarabit, and the Jabal Gasus corridor. Although high F-parameter values may occur in hydrothermally modified rocks [57,82,91], this parameter combines K abundance and the eU/eTh ratio and is not specific to potassic alteration. Its regional distribution is therefore evaluated first against the mapped felsic and sedimentary units. Coincidence with lineament concentrations and documented mineral occurrences strengthens the rationale for field follow-up but does not independently establish hydrothermal fluid flow or alteration.

The Kd map (Figure 9b) expresses potassium enrichment or depletion relative to the selected K–eTh background relationship, rather than identifying an alteration assemblage [28]. Positive Kd values may reflect primary K-rich lithologies or localized K addition; negative values may reflect K-poor lithologies, K loss, or surface-material effects. Neither sign alone establishes alteration type or intensity [83,92]. Consequently, sericitization, chloritization, and potassic alteration are not assigned from Kd values without independent mineralogical evidence. The localized eU responses in Figure 10d are likewise interpreted in their geological context. Anomalies near phosphatic and sedimentary units are consistent with the previously reported uranium enrichment of Duwi Formation phosphorites [45,93], and are not treated as evidence of hydrothermal mineralization [83,92]. Local alignment with faults, contacts, or drainage corridors identifies sites where secondary redistribution could be investigated but does not establish its origin. The eU-composite map (Figure 10d) is the most geochemically and structurally variable of the radiometric derivatives. U-rich zones arise in the eastern and central sectors, but their distribution is more locally and patchily aligned with the main wadi, faults, and contact corridors. This pattern indicates secondary U redistribution by oxidizing fluids along permeable structural paths, rather than only the primary lithological rule. The nearness of some eU anomalies to sedimentary and phosphatic units is compatible with the results of Zoheir and Akawy [93], who reported U enrichment (90–152 ppm) in the Duwi Formation phosphorites, and with El Qassas et al. [45], who recognized the Duwi Formation as a high-radioactivity unit. The radioelements map (Figure 10a) incorporates eU, K, and eTh into a single visualization that strengthens the performance of composite possible alteration, lithological, and structural controls. The central-eastern parts are dominated by combined potassium-rich coloring signatures, suggesting a stronger contribution from altered felsic lithologies and K-bearing units, whereas the western part is differentiated by darker cyan-blue-green colors, compatible with low radiometric responses from mafic-ultramafic rock units. This pattern matches the geological allocation and is additionally supported by the

petrological description of Luo et al. [65], who noted the calc-alkaline association and island-arc framework of the metavolcanics in the adjoining Abu Marawat region.

The fuzzy mineral prospectivity model (Figure 11), incorporating lithological, radiometric, and structural evidence, highlights regional screening domains for follow-up exploration. The association of high scores with lithological contacts and structural intersections is compatible with favorable settings for fluid focusing, but does not independently demonstrate hydrothermal overprinting [62,84]. The most heightened prospectivity values are concentrated in the eastern and central parts (parts of W. Abu Aqarib, Jabal Gasus, Jabal Umm Zarabit, and W. Abu Safi), where the mineral system features are optimally developed. Because phosphate mineralization in the Duwi Formation is of syn-sedimentary, basinal origin rather than epigenetic hydrothermal origin, phosphate occurrences are excluded from the AUC and success-rate calculations used for internal assessment of the hydrothermal/structural prospectivity model. Their spatial distribution, concentrated in areas of low magnetic lineament density and moderate radiometric response (Section 4, Results), is consistent with a stratigraphic rather than structural control, and their presence in lower-scoring zones of the fuzzy map should not be interpreted as a model failure. Where phosphate occurrences do coincide with highly favorable zones, this is considered a coincidental spatial overlap rather than a validation of the hydrothermal targeting criteria. The model is tailored to hydrothermal styles of structurally controlled gold and intrusion-related mineralization, and performs less well for the other mineralization types of the district. High scores may therefore reflect hydrothermal mineralization styles (e.g., gold), and the less favorable occurrences may belong to a style not represented by the four layers. Classifying the documented occurrences by commodity and deposit style (Table 1) and refining the layers for each style should follow when more occurrences are available. The integrated geophysical framework applied in this investigation offers a data-driven, objective basis for exploration targeting in the Jabal Gasus region and similar terrains globally. By narrowing the search space to structurally and geochemically favorable corridors ahead of ground follow-up, this strategy has the potential to reduce exploration risk and environmental disturbance relative to untargeted or purely grid-based drilling programs; however, this study does not quantify such reductions, and realizing this benefit would depend on how the ranked targets are incorporated into an actual field exploration program.

A small number of documented occurrences fall within the poorly favorable class (n = 2, corresponding to 28.57% of total occurrences). These cases may reflect: (i) evidence-layer resolution limits, since the 250 m TMI grid cell size and the coarse radiometric traverse-line spacing (1.0 km) may not capture narrow, high-grade veins or small intrusive bodies below the effective resolution of the survey; (ii) occurrences controlled by lithological or structural factors not captured by the four evidence layers used here (e.g., stratigraphic or unconformity-related controls not expressed as lineament density, F-parameter, CFT anomalies, or the reclassified lithology layer); (iii) minor positional uncertainty in the occurrence locations relative to the underlying grids or (iv) occurrences associated with weakly expressed alteration that falls below the linear membership thresholds adopted for the F-parameter and CFT layers. These outliers do not invalidate the overall model performance but indicate that the current evidence layers should be regarded as a first-pass regional screening tool rather than a guarantee of exhaustive detection at the individual-deposit scale. The model performed best for gold, as gold occurrences fall in the highly favorable class. Because this class covers 62.53% of the area, this capture is consistent with a useful but modest targeting performance. The molybdenum and polymetallic occurrences lie mostly near or more than 1 km from the high-score zones. This result is expected from the choice of evidence layers: lineament density, the F-parameter, lithology, and, to a lesser extent, the CET-PA circular features represent structurally controlled gold

in felsic and metavolcanic host rocks, whereas molybdenum in intrusion-related systems would need evidence of the causative intrusion and its alteration, and the syn-sedimentary phosphate in the Duwi Formation is controlled by stratigraphy and is excluded from the model. The workflow is therefore tailored to structurally controlled gold and is not a one-size-fits-all method.

The highly favorable class covers 62.53% of the area and is therefore a broad screening domain and not a drill-ready target. Its breadth reflects the combined evidence of the four layers in an area where felsic basement rocks, which receive high lithology scores, are widespread, and the gamma value of 0.90, which gives high scores to cells with moderate support in several layers. The equal weighting of partly related layers (the F-parameter and the lithology layer, and lineament density and the CET-PA score) may also contribute; alternative weights were not tested. The class contains 71.43% of the hydrothermal occurrences (1.14 times its area share), so its selectivity is modest, and the highest-scoring part of the class is proposed for first-priority follow-up.

The results of our study contribute to a more comprehensive understanding of the affinity between structural evolution and mineralization in the ENS and similar collisional orogens. The history of polyphase deformation, as demonstrated by Eldosouky et al. [86], provides the structural framework for the evolution of mineral systems. The structural regime of mineralization is not invariant but changes with tectonic phase. The NW shear zones, associated with the Najd Fault System [4,10,94,95], control gold quartz veins in Massaghat, Rodruin, and Semna, while N-S shear zones influence mineralization at Abu Gaharish, Gidami, Mirinda, and Abu Marawat [86–89,96]. This spatial partitioning indicates that various deformation stages formed distinct structural pathways for fluid flow, consistent with the statements of Groves et al. [71] regarding the structural architecture of orogenic gold deposits. The radiometric signatures provide complementary constraints on lithological variation and identify local anomalies for follow-up assessment. Elevated K and eU responses in the central–eastern domain are consistent with the distribution of felsic and sedimentary units, but do not independently establish a magmatic metal source, hydrothermal convection, or alteration. Uranium enrichment associated with phosphatic units is considered separately in its sedimentary context [93].

Data Limitations and Uncertainties

The nominal 1 km survey-line spacing is consistent with the regional focus of the study, while interpolation to a 250 m grid facilitates spatial analysis and visualization without changing the underlying sampling resolution. Interpretation, therefore, emphasizes broader structural patterns, with smaller features requiring higher-resolution follow-up. As the available dataset comprised an archived processed grid rather than the original flight-line observations and positions, local sampling coverage and potential gridding or levelling effects may influence the assessment of individual small features.

Magnetic lineaments and circular anomalies provide regional-scale constraints on possible structural boundaries and intrusive features, supporting exploration-target prioritization. Euler-derived source locations and depths complement this framework and are interpreted in the context of the assumed structural indices, window size, derivative quality and possible source interference, without implying uniquely resolved fault depths or deep-crustal connectivity. The study emphasizes regional screening rather than magnetic inversion; subsequent constrained inversion could further refine source geometry. Radiometric patterns principally reflect lithological variation, while the F-parameter and Kd provide complementary indicators of possible alteration when evaluated alongside geological and structural evidence.

The fuzzy model provides a knowledge-driven favorability ranking whose results depend on evidence-layer selection, membership assignments, equal weighting, and class

thresholds. Some evidence layers capture related geological characteristics, which may contribute to the spatial extent of elevated scores. The highly favorable class, covering 62.53% of the study area, represents a regional exploration-screening domain within which the highest-scoring sectors can be prioritized for detailed follow-up. The AUC of 0.733 indicates encouraging agreement between the prospectivity ranking and the seven documented hydrothermal occurrences. As these occurrences also informed gamma selection, the result represents an internal assessment; additional independent occurrences would allow further evaluation of predictive performance. The correspondence is strongest for gold and does not support successful prediction of molybdenum or phosphate mineralization. Consequently, the ranked sectors require geological, geochemical, and ground-geophysical verification, and application to other deposit types requires appropriately selected evidence layers and separate evaluation. The highly favorable class covers 62.53% of the area and is therefore a broad screening domain. The AUC (0.733) is based on seven hydrothermal occurrences and is a success-rate measure because the same occurrences were used. Five of the seven occurrences fall in the highly favorable class, whereas the phosphate occurrences lie mostly more than 1 km from the high-score zones, so the workflow is tailored to structurally controlled gold and is not a one-size-fits-all method. The map is a first-pass screening ranking that should be combined with mapping, geochemistry, and ground geophysics before drilling.

6. Conclusions

This study identifies N-S, NW-SE, and NE-SW magnetic lineaments, lithological contacts, and intrusive-related anomalies that are spatially associated with known mineral occurrences and radiometric indicators. Euler deconvolution under alternative structural-index assumptions provides supporting, model-dependent estimates of magnetic-source depth and location. These results are most appropriately used to prioritize structurally complex corridors for follow-up exploration, rather than to establish unique fault depths, deep-crustal connectivity, or mantle-derived fluid sources. Integration of high resolution aeromagnetic and aeroradiometric datasets with IL and LSF edge detection filters, CET GA/CET PA, Euler deconvolution, and fuzzy logic prospectivity modeling resolves the structural architecture and delineates discrete, well-defined corridors of high prospectivity. These corridors coincide with intrusive centers, radiometric anomalies, and documented gold, polymetallic, and molybdenum occurrences, thereby supporting the mineral system interpretation, although this does not constitute independent validation of the model. Phosphate occurrences are excluded from the model evaluation. Radiometric derivatives and ternary composites identify radioelement contrasts associated principally with felsic, mafic–ultramafic, volcanic, and sedimentary lithologies. Local F-parameter, eU, and potassium-deviation anomalies that coincide with favorable structures and documented occurrences represent prospective sites for follow-up assessment of possible hydrothermal alteration. The fuzzy prospectivity model successfully synthesizes structural, lithological, and radiometric indicators into a knowledge-driven, first-pass ranking surface that highlights central–eastern domains for follow-up. The AUC of 0.733 is an internal success-rate measure, not independent validation, because the same seven occurrences guided gamma selection and assessment. The proposed workflow provides a transferable approach to early-stage target prioritization in Precambrian terranes. The map can support reconnaissance planning, but the broad, highly favorable class is not a set of drill-ready targets. Finer-scale prioritization requires geological mapping, geochemistry, alteration studies, and ground geophysics, and independent testing and field follow-up are needed to confirm exploration efficiency. Application elsewhere would require local calibration. Whether this sequencing reduces drilling or environmental disturbance was not

measured and would depend on the baseline exploration design, access conditions, target depth, permitting requirements, and the results of field verification.

Supplementary Materials: The following supporting information can be downloaded at: https://www.mdpi.com/article/10.3390/min16111099/s1.

Author Contributions: Conceptualization, A.M.E., M.N., E.S.R.L., H.A., and F.A.; methodology, M.N., A.M.E., S.P.O., E.S.R.L., M.S. (Mabrouk Sami), and F.A.; software, M.N., A.M.E.; validation, M.N., A.M.E., E.S.R.L., M.S. (Mabrouk Sami), and F.A.; formal analysis, M.N., A.M.E., E.S.R.L., S.P.O., and F.A.; investigation, A.M.E., M.N., E.S.R.L., M.S. (Mabrouk Sami), and F.A.; resources, M.N., A.M.E., M.S. (Mohamed Salaheldin), and F.A.; data curation, M.N., A.M.E., and M.S. (Mohamed Salaheldin); writing—original draft preparation, M.N., A.M.E., H.A., M.S. (Mabrouk Sami), S.P.O., and F.A.; writing—review and editing, all authors; visualization, M.N., A.M.E., E.S.R.L., H.A., M.S. (Mabrouk Sami), M.S. (Mohamed Salaheldin), S.P.O., and F.A.; supervision, M.N., A.M.E., and F.A.; project administration, A.M.E., and M.N.; funding acquisition, A.M.E., M.N., E.S.R.L., and F.A. All authors have read and agreed to the published version of the manuscript.

Funding: The authors extend their appreciation to the King Saud University for funding through Ongoing Research Funding program (ORF-2026-1120), King Saud University, Riyadh, Saudi Arabia. S.P.O was supported by National Council for Scientific and Technological Development - CNPq, grant number 306516/2024-1.

Data Availability Statement: The geophysical data used in this study are archived in a DOI-assigning repository: https://doi.org/10.5281/zenodo.22815124. The repository includes the data and processing information required to support the reported analyses. Supplementary Table S1 provides the Fuzzy membership parameters for all evidence layers. Supplementary Table S2 provides the Lithology membership scores (categorical layer). Supplementary Table S3 summarizes the evidence layers, derived parameters, and their roles in the workflow.

Conflicts of Interest: The authors declare no conflicts of interest.

References

1. Said, R. *The Geology of Egypt*, 1st ed.; Routledge: London, UK, 1990.
2. El Ghrabawy, O.; Soliman, N.; Tarshan, A. Remote sensing signature analysis of ASTER imagery for geological mapping of Gasus area, central eastern desert, Egypt. *Arab. J. Geosci.* **2019**, *12*, 408. https://doi.org/10.1007/s12517-019-4531-9.
3. Hamimi, Z.; Abd El-Wahed, M.A. Suture and major shear zones in the Neoproterozoic basement of Egypt. In *The Geology of Egypt*; Fritz, H., Ed.; Springer International Publishing: Cham, Switzerland, 2020; pp. 153–189.
4. Hamimi, Z.; Eldosouky, A.M.; Hagag, W.; Kamh, S.Z. Large-scale geological structures of the Egyptian Nubian Shield. *Sci. Rep.* **2023**, *13*, 1923.
5. Zaki, O.A.; AbdAlnabi, S.H.; Abd El Wahab, S.E.; Ismail, A.A.; Soliman, N.M. Aeromagnetic signature analysis of Gasus area and its surroundings, Central Eastern Desert, Egypt. *Arab. J. Geosci.* **2017**, *10*, 310. https://doi.org/10.1007/s12517-017-3100-3.
6. Abraham, E.M.; Uwaezuoke, A.E.; Usman, A.O. Geophysical investigation of subsurface mineral potentials in North-Central Nigeria: Implications for sustainable mining and development. *Geomech. Geophys. Geo-Energy Geo-Resour.* **2024**, *10*, 192. https://doi.org/10.1007/s40948-024-00913-3.
7. Usman, A.O.; Abraham, E.M.; Okonkwo, C.C.; Augustine, I.C.; Azuoko, G.-B. Geothermal energy appraisal and subsurface structural mapping of the Rafin Rewa Warm Spring region, Precambrian basement complex of Nigeria. *Sci. Rep.* **2024**, *14*, 17368. https://doi.org/10.1038/s41598-024-66927-9.
8. Mohamed, H.; Saibi, H.; Bersi, M.; Abdelnabi, S.; Geith, B.; Ismaeil, H.; Tindell, T.; Mizunaga, H. 3-D magnetic inversion and satellite imagery for the Um Salatit gold occurrence, Central Eastern Desert, Egypt. *Arab. J. Geosci.* **2018**, *11*, 674. https://doi.org/10.1007/s12517-018-4020-6.
9. Eldosouky, A.M.; Pham, L.T.; Henaish, H. High precision structural mapping using edge filters of potential field and remote sensing data: A case study from Wadi Umm Ghalqa area, South Eastern Desert, Egypt. Egypt. J. Remote Sens. Space Sci. 2022, 25, 501–513. https://doi.org/10.1016/j.ejrs.2022.03.001

10. Betts, P.G.; Moore, D.; Aitken, A.; Blaikie, T.; Jessell, M.; Ailleres, L.; Armit, R.; McLean, M.; Munukutla, R.; Chukwu, C. Geology from aeromagnetic data. *Earth-Sci. Rev.* **2024**, *258*, 104958. https://doi.org/10.1016/j.earscirev.2024.104958.
11. Abraham, E.M.; Onwe, M.R.; Usman, A.O.; Gwazah, C.A.; Uchenna, M.E. Mapping of mineral deposits within granitic rocks by aeromagnetic data-a case study from Northern Nigeria. *Arab. J. Geosci.* **2022**, *15*, 1656. https://doi.org/10.1007/s12517-022-10947-0.
12. Wang, L.; Zhang, Y.; Han, R.; Li, X. LA-ICP-MS analyses of trace elements in zoned sphalerite: A study from the Maoping carbonate-hosted Pb-Zn(-Ge) deposit, southwest China. *Ore Geol. Rev.* **2023**, *157*, 105468. https://doi.org/10.1016/j.oregeorev.2023.105468.
13. Han, R.; Wu, J.; Zhang, Y.; Chen, Q.; Sun, B. Oblique distribution patterns and the underlying mechanical model of orebody groups controlled by structures at different scales. *Sci. Rep.* **2024**, *14*, 4591. https://doi.org/10.1038/s41598-024-55473-z.
14. Essa, K.S.; Elhussein, M. PSO (particle swarm optimization) for interpretation of magnetic anomalies caused by simple geometrical structures. *Pure Appl. Geophys.* **2018**, *175*, 3539–3553. https://doi.org/10.1007/s00024-018-1867-0.
15. El-Badrway, H.; Alrefaee, H.; Nagy, M. Elicitation of the tectonic shearing structures in the northeastern part of Sirt Basin, Libya, as deduced by potential field data. *Egypt. J. Geol.* **2023**, *67*, 71–86.
16. Li, Y.; Oldenburg, D.W. 3-D inversion of magnetic data. *Geophysics* **1996**, *61*, 394–408. https://doi.org/10.1190/1.1443968.
17. Pham, L.T. An improved edge detector for interpreting potential field data. *Earth Sci. Inform.* **2024**, *17*, 2763–2774. https://doi.org/10.1007/s12145-024-01286-7.
18. Abdelwahed, M.; Abdelazeem, M.; Eldougdoug, A.A.; Gobashy, M.M.; Abd El-Rahman, Y.M.; Said, S.; Abdelhalim, A. Remote sensing and magnetic characterization of the Au mineralization and its structural implications: Meatiq dome, Eastern Desert, Egypt. *J. Afr. Earth Sci.* **2024**, *220*, 105442. https://doi.org/10.1016/j.jafrearsci.2024.105442.
19. Cordell, L.; Grauch, V.J.S. Mapping basement magnetization zones from aeromagnetic data in the San Juan Basin, New Mexico. In *The Utility of Regional Gravity and Magnetic Maps*; Hinze, W.J., Ed.; Society of Exploration Geophysicists: Tulsa, OK, USA, 1985; pp. 181–197. https://doi.org/10.1190/1.0931830346.ch16.
20. Miller, H.G.; Singh, V. Potential field tilt: A new concept for location of potential field sources. *J. Appl. Geophys.* **1994**, *32*, 213–217. https://doi.org/10.1016/0926-9851(94)90022-1.
21. Roest, W.R.; Verhoef, J.; Pilkington, M. Magnetic interpretation using the 3-D analytic signal. *Geophysics* **1992**, *57*, 116–125.
22. Hsu, S.K.; Coppense, D.; Shyu, C.T. High-resolution detection of geologic boundaries from potential field anomalies: An enhanced analytic signal technique. *Geophysics* **1996**, *61*, 1947–1957.
23. Pham, L.T.; Van Vu, T.; Le Thi, S.; Trinh, P.T. Enhancement of potential field source boundaries using an improved logistic filter. *Pure Appl. Geophys.* **2020**, *177*, 5237–5249. https://doi.org/10.1007/s00024-020-02542-9.
24. Wijns, C.; Perez, C.; Kowalczyk, P. Theta map: Edge detection in magnetic data. *Geophysics* **2005**, *70*, L39–L43.
25. Verduzco, B.; Fairhead, J.D.; Green, C.M.; MacKenzie, C. New insights into magnetic derivatives for structural mapping. *Lead. Edge* **2004**, *23*, 116–119. https://doi.org/10.1190/1.1651454.
26. Cooper, G.R.J.; Cowan, D.R. Edge enhancement of potential-field data using normalized statistics. *Geophysics* **2008**, *73*, H1–H4. https://doi.org/10.1190/1.2837309.
27. Holden, E.J.; Wedge, D.; Kovesi, P.; Dentith, M.; Miller, S. Detection of regions of structural complexity within aeromagnetic data using image analysis. In Proceedings of the 25th International Conference on Image and Vision Computing New Zealand, Queenstown, New Zealand, 8–9 November 2010; pp. 1–6.
28. Akingboye, A.S.; Bery, A.A.; Ogunyele, A.C.; Dick, M.D.; Ale, T.O.; Titus, E.A. Correction: Magnetic-Assisted Radiometric, Speciation, and Environmental Studies of an Orogenic Gold Terrain: Okpella, Igarra Schist Belt, SW Nigeria. *Earth Syst. Environ.* **2025**, *9*, 2643. https://doi.org/10.1007/s41748-025-00704-0.
29. International Atomic Energy Agency. *Guidelines for Radioelement Mapping Using Gamma Ray Spectrometry Data*; International Atomic Energy Agency: Vienna, Austria, 2003.
30. Sabra, M.E.M.; Abdeldayem, A.L.; Youssef, M.A.S.; Masoud, A.A.; Mansour, S.A. Determination of the radiation dose rate and radiogenic heat production of North Gabal Abu Hibban area, central Eastern Desert Egypt. *NRIAG J. Astron. Geophys.* **2019**, *8*, 103–111. https://doi.org/10.1080/20909977.2019.1617556.
31. Amer, R.; El Mezayen, A.; Hasanein, M. ASTER spectral analysis for alteration minerals associated with gold mineralization. *Ore Geol. Rev.* **2016**, *75*, 239–251. https://doi.org/10.1016/j.oregeorev.2015.12.008.
32. Ghoneim, S.M.; Ali, H.F.; Abdelrahman, K.; Fnais, M.S.; Lala, A.M.S. Integrating remote sensing and geophysical data for mapping potential gold mineralization localities at Abu Marawat area, central Eastern Desert, Egypt. *Sci. Rep.* **2024**, *14*, 18273. https://doi.org/10.1038/s41598-024-68921-7.

33. Holden, E.J.; Wong, J.C.; Kovesi, P.; Wedge, D.; Dentith, M.C.; Bagas, L. Identifying structural complexity in aeromagnetic data: An image analysis approach to greenfields gold exploration. *Ore Geol. Rev.* **2012**, *46*, 47–59. https://doi.org/10.1016/j.oregeorev.2011.11.002.
34. Reid, A.B.; Allsop, J.M.; Granser, H.; Millet, A.J.; Somerton, I.W. Magnetic interpretations in three dimensions using Euler deconvolution. *Geophysics* **1990**, *55*, 80–91. https://doi.org/10.1190/1.1442774.
35. Nagy, M., Eldosouky, A.M. Advanced Targeting of Rare Earth Elements in the Gabal Umm Naggat Pluton: A Combined Geophysical and Radiogenic Approach with Mineralization and Environmental Implications. Nat. Resour. Res. 2026. https://doi.org/10.1007/s11053-026-10698-9.
36. Hume, W.F. *Geology of Egypt*; Part 11; The Geological Survey of Egypt: Cairo, Egypt, 1937; Volume 11.
37. El-Bialy, M.Z. Precambrian Basement Complex of Egypt. In *The Geology of Egypt. Regional Geology Reviews*; Hamimi, Z., El-Barkooky, A., Martínez Frías, J., Fritz, H., Abd El-Rahman, Y., Eds.; Springer: Cham, Switzerland, 2020; pp. 37–79. https://doi.org/10.1007/978-3-030-15265-9_2.
38. Kamel, M.; Abdeen, M.M.; Youssef, M.M.; Orabi, A.M.; Abdelbaky, E. Utilization of Landsat-8 (OLI) Image Data for Geological Mapping of the Neo-Proterozoic Basement Rocks in the Central Eastern Desert of Egypt. *J. Indian Soc. Remote Sens.* **2022**, *50*, 469–492. https://doi.org/10.1007/s12524-021-01465-9.
39. Hamimi, Z.; Fowler, A.R.; Liégeois, J.P.; Collins, A.; Abdelsalam, M.G.; Abd El-Wahed, M. (Eds.) *The Geology of the Egyptian Nubian Shield*; Regional Geology Reviews; Springer Nature: Cham, Switzerland, 2021.
40. Yousif, M.; Sracek, O. An overview of phosphate rocks and their mining impact on groundwater, Eastern Desert, Egypt. *Arab. J. Geosci.* **2016**, *9*, 670. https://doi.org/10.1007/s12517-016-2698-x.
41. Salahel-Din, K. Estimation of heat generation by radioactive decay of some phosphate rocks in Egypt. *Appl. Radiat. Isot.* **2009**, *67*, 2033–2036. https://doi.org/10.1016/j.apradiso.2008.10.016.
42. Gaafar, I.; Abu El Ghar, M.; Ibrahim, T.; Diab, M. Mineralogy and ground gamma-ray spectrometric investigation for phosphates of Gabal Abu Had area, Central Eastern Desert, Egypt. *NRIAG J. Astron. Geophys.* **2020**, *9*, 375–392. https://doi.org/10.1080/20909977.2020.1746893.
43. Fritz, H.; Abdelsalam, M.; Ali, K.A.; Bingen, B.; Collins, A.; Fowler, A.; Ghebreab, W.; Hauzenberger, C.; Johnson, P.; Kusky, T.; et al. Orogen styles in the East African Orogen: A review of the Neoproterozoic to Cambrian tectonic evolution. *J. Afr. Earth Sci.* **2013**, *86*, 65–106. https://doi.org/10.1016/j.jafrearsci.2013.06.004.
44. Abd El-Rahman, Y.; Helmy, H.M.; Surour, A.A.; Maurice, A.E.; Abu El-Rus, M.A. Orogenic lode-gold deposits and listvenization processes in the El-Barramiya area, Eastern Desert, Egypt. *Environ. Earth Sci.* **2023**, *82*, 420. https://doi.org/10.1007/s12665-023-11083-y.
45. El Qassas, R.A.Y.; Salaheldin, M.; Assran, S.M.A.; Abdel Fattah, T.; Rashed, M.A. Airborne gamma-ray spectrometric data interpretation on Wadi Queih and Wadi Safaga area, Central Eastern Desert, Egypt. *NRIAG J. Astron. Geophys.* **2020**, *9*, 155–167. https://doi.org/10.1080/20909977.2020.1728893.
46. Aero-Service. *Final Operational Report of Airborne Magnetic/Radiation Survey in the Eastern Desert, Egypt*; prepared for the Egyptian General Petroleum Corporation (EGPC) and the Egyptian Geological Survey and Mining Authority (EGSMA); Aero-Service Division, Western Geophysical Company of America: Houston, TX, USA, 1984.
47. Macleod, I.N.; Vieira, S.; Chaves, A.C. Analytic Signal and Reduction-to-the-Pole in the Interpretation of Total Magnetic Field Data at Low Magnetic Latitudes. In Proceedings of the Third International Congress of the Brazilian Society of Geophysics, Rio de Janeiro, Brazil, 7–11 November 1993; pp. 7–11. https://doi.org/10.3997/2214-4609-pdb.324.830.
48. El-Badrawy, H.T.; Abbas, A.M.; Massoud, U.; Abu-Alam, T.; Alrefaee, H.A.; Abo Khashaba, S.M.; Nagy, M. Integrated approach-based groundwater mapping in Sohag Governorate, Upper Egypt, using remote sensing and aeromagnetic data. *Front. Earth Sci.* **2024**, *12*, 1456055. https://doi.org/10.3389/feart.2024.1456055.
49. El-Badrawy, H.T.; Abo Khashaba, S.M.; Araffa, S.A.S.; Kassab, M.; Nagy, M. Mapping and predicting groundwater accumulations using remote sensing and aeromagnetic data: A case study from Bahariya Oasis, Western Desert, Egypt. *Sci. Rep.* **2026**, *16*, 10489. https://doi.org/10.1038/s41598-026-42907-z.
50. Melouah, O.; Pham, L.T. Improved ILTHG method for edge enhancement of geological structures: Application to gravity data from the Oued Righ Valley. *J. Afr. Earth Sci.* **2021**, *177*, 104162 https://doi.org/10.1016/j.jafrearsci.2021.104162.
51. Pham, L.T.; Eldosouky, A.M.; Oksum, E.; Saada, S.A. A new high resolution filter for source edge detection of potential data. *Geocarto Int.* **2022**, *37*, 3051–3068. https://doi.org/10.1080/10106049.2020.1849414.
52. Pham, L.T.; Oksum, E.; Do, T.D.; Le-Huy, M. New method for edges detection of magnetic sources using logistic function. *Geofiz. Zhurnal* **2018**, *40*, 127–135. https://doi.org/10.24028/gzh.0203-3100.v40i6.2018.151033.

53. Eldosouky, A.M.; Saada, S.A.; Allam, S.A.; Abd El-Gawad, A.; Henaish, A.; Zamzam, S. A robust edge-detection approach for precise delineation of deep structures from potential field data: Structural insights supported by remote sensing. *Sci. Rep.* **2025**, *15*, 38475. https://doi.org/10.1038/s41598-025-23678-5.
54. Thompson, D.T. EULDPH: A new technique for making computer-assisted depth estimates from magnetic data. *Geophysics* **1982**, *47*, 31–37. https://doi.org/10.1190/1.1441278.
55. Hasan, A.N.; Nagy, M.; Ahmed, M.A.; El-Meselhy, A. Integrating remote sensing, GIS, and magnetic geophysics for the evaluation of mineral resources in the Bahariya-Farafra region, Western Desert, Egypt, for industrial development. *Egypt. J. Geol.* **2024**, *68*, 417–435.
56. Holden, E.J.; Fu, S.C.; Kovesi, P.; Dentith, M.; Bourne, B.; Hope, M. Automatic identification of responses from porphyry intrusive systems within magnetic data using image analysis. *J. Appl. Geophys.* **2011**, *74*, 255–262. https://doi.org/10.1016/j.jappgeo.2011.06.016.
57. Abd El Nabi, S.H. An analysis of airborne gamma ray spectrometric data of Gabal Umm Naggat granitic pluton, Central Eastern Desert, Egypt. *JAKU Earth Sci.* **2012**, *23*, 19–42.
58. Achkouch, L.; Miftah, A.; Ouchchen, M.; Mamouch, Y.; Attou, A.; Boutaleb, S.; Dadi, B. Mapping and litho-geophysical classification of potential mining areas by spatial remote sensing and helicopter-borne gamma-ray spectrometry (Tikirt, Anti-Atlas, Morocco). *Geophys. Prospect.* **2023**, *71*, 1551–1569. https://doi.org/10.1111/1365-2478.13376.
59. Ordóñez, C.; Ekwok, S.E.; Alkhayaat, A.; Bains, P.S.; Sharma, R.; Kumar, R.; Kulshreshta, A.; Mann, V.S.; Elmasry, Y. Delineation of mineralization-related geologic structures and lithological units using airborne magnetic and radiometric data. *Geomech. Geophys. Geo-Energ. Geo-Resour.* **2024**, *10*, 184. https://doi.org/10.1007/s40948-024-00902-6.
60. Mohamed, W.H.; Alhazani, T.; Sabra, M.E.M.; El-Badry, B.A.; Sami, M.; Sanislav, I.V.; Lasheen, E.S.R. Delineation of subsurface structure and radiological hazards utilizing integrated airborne magnetic and spectrometric data. J. Radiat. Res. Appl. Sci. 2026, 19, 102489. https://doi.org/10.1016/j.jrras.2026.102489.
61. Zadeh, L.A. Fuzzy sets. *Inf. Control* **1965**, *8*, 338–353.
62. Nykänen, V.; Niiranen, T.; Molnár, F.; Lahti, I.; Korhonen, K.; Cook, N.; Skyttä, P. Optimizing a knowledge-driven prospectivity model for gold deposits within Peräpohja Belt, Northern Finland. *Nat. Resour. Res.* **2017**, *26*, 571–584. https://doi.org/10.1007/s11053-016-9321-4.
63. Nykänen, V.; Törmänen, T.; Niiranen, T. Cobalt prospectivity using a conceptual fuzzy logic overlay method enhanced with the mineral systems approach. *Nat. Resour. Res.* **2023**, *32*, 2387–2416. https://doi.org/10.1007/s11053-023-10255-8.
64. Blakely, R.J. *Potential Theory in Gravity and Magnetic Applications*, 1st ed.; Cambridge University Press: Cambridge, UK, 1996; 441p. https://doi.org/10.1017/CBO9780511549816.
65. Luo, T.; El-Din, G.K.; Osman, I.; Abdelkareem, M. Geochemistry and tectonic setting of the Abu-Marawat metavolcanics, Central Eastern Desert—Egypt. *Arab. J. Geosci.* **2020**, *13*, 1056. https://doi.org/10.1007/s12517-020-06051-w.
66. Jacobsen, H.A. Case for upward continuation as a standard separation filter for potential-field maps. *Geophysics* **1987**, *52*, 1138–1148. https://doi.org/10.1190/1.1442378.
67. Nagy, M.; Hussein, M.; Boghdady, S.; Abo Khashaba, S.M. Advanced multi-technique aeromagnetic and remote sensing characterization of a small-scale gold prospect: A case study from the Um Salim area. *Sci. Rep.* **2026**, *16*, 18858. https://doi.org/10.1038/s41598-026-57415-3.
68. Abo Khashaba, S.M.; Hassan, S.M.; Sadek, M.F.; Laban, N.; Gabr, S.S.; Metwalli, M.R.; Sami, M.; Alhejji, S.S.; Sanislav, I.V.; Nagy, M. Integrated remote sensing and aeromagnetic datasets for mapping iron mineralization potential in the El-Bahariya depression in the Western Desert of Egypt. *Sci. Rep.* **2026**, *16*, 19600. https://doi.org/10.1038/s41598-026-59828-6.
69. Nabighian, M.N.; Grauch, V.J.S.; Hansen, R.O.; LaFehr, T.R.; Li, Y.; Peirce, J.W.; Phillips, J.D.; Ruder, M.E. The historical development of the magnetic method in exploration. *Geophysics* **2005**, *70*, 33ND–61ND. https://doi.org/10.1190/1.2133784.
70. Pham, L.T.; Eldosouky, A.M.; Melouah, O.; Abdelrahman, K.; Alzahrani, H.; Oliveira, S.P.; Andráš, P. Mapping subsurface structural lineaments using the edge filters of gravity data. *J. King Saud Univ. Sci.* **2021**, *33*, 101594.
71. Groves, D.I.; Santosh, M.; Goldfarb, R.J.; Zhang, L. Structural geometry of orogenic gold deposits: Implications for exploration of world-class and giant deposits. *Geosci. Front.* **2018**, *9*, 1163–1177. https://doi.org/10.1016/j.gsf.2018.01.006.
72. Holden, E.J.; Dentith, M.; Kovesi, P. Towards the automatic analysis of regional aeromagnetic data to identify regions prospective for gold. *Comput. Geosci.* **2008**, *34*, 1505–1513. https://doi.org/10.1016/j.cageo.2007.08.007.
73. Aitken, A.R.; Betts, P.G. High-resolution aeromagnetic data over central Australia assist Grenville-era (1300–1100 Ma) Rodinia reconstructions. *Geophys. Res. Lett.* **2008**, *35*, L01306. https://doi.org/10.1029/2007GL031563.

74. McCuaig, T.C.; Hronsky, J.M.A. *The Mineral System Concept: The key to Exploration Targeting*; Society of Economic Geologists Special Publications; SEG: Littleton, CO, USA, 2014; Volume 18, pp. 153–175.
75. Arogundade, A.B.; Awoyemi, M.O.; Ajama, O.D.; Falade, S.C.; Hammed, O.S.; Dasho, O.A.; Adenika, C.A. Integrated aeromagnetic and airborne radiometric data for mapping potential mineralisation zones in parts of Zamfara, northwest Nigeria. *Pure Appl. Geophys.* **2022**, *179*, 351–369. https://doi.org/10.1007/s00024-021-02913-w.
76. Mostafa, M.S.; Salam, H.F.A.E.; Shaheen, M.A.; Abdel Gawad, A.E. Delineation of radioactive and mineralized zones in NE Desert of Egypt: Integration of structural analysis and airborne geophysical data. *Arab. J. Geosci.* **2026**, *19*, 96 https://doi.org/10.1007/s12517-026-12461-z.
77. Alvandi, A.; Ghanati, R. Using magnetic data for estimating the location of lateral boundaries and the depth of the shallow salt dome of Aji Chai, East Azerbaijan Province, Iran. *Int. J. Min. Geo-Eng.* **2023**, *57*, 251–258.
78. Gaafar, I.; Elbarbary, M.; Sayyed, M.I.; Sulieman, A.; Tamam, N.; Khandaker, M.U.; Bradley, D.A.; Hanfi, M.Y. Assessment of Radioactive Materials in Albite Granites from Abu Rusheid and Um Naggat, Central Eastern Desert, Egypt. *Minerals* **2022**, *12*, 120. https://doi.org/10.3390/min12020120.
79. Wilford, J.R.; Bierwirth, P.N.; Craig, M.A. Application of airborne gamma-ray spectrometry in soil/regolith mapping and applied geomorphology. *AGSO J. Aust. Geol. Geophys.* **1997**, *17*, 201–216.
80. El-Anwar, E.A.A.; El Rahim, S.H.A. Mineralogy, geochemistry and origin of the phosphorites at Um El-Huwtat mine, Quseir, Central Eastern Desert, Egypt. *Carbonates Evaporites* **2022**, *37*, 16. https://doi.org/10.1007/s13146-022-00759-4.
81. Minty, B.R.S. Fundamentals of airborne gamma-ray spectrometry. *AGSO J. Aust. Geol. Geophys.* **1997**, *17*, 39–50.
82. Hezarkhani, A. Geochemical element mobility during alteration/mineralization in the Sungun porphyry copper deposit, Azerbaijan–Iran. *Int. Geol. Rev.* **2011**, *53*, 980–1002. https://doi.org/10.1080/00206811003683192.
83. Sanusi, S.O.; Amigun, J.O. Structural and hydrothermal alteration mapping related to orogenic gold mineralization in part of Kushaka Schist Belt, North-Central Nigeria, using airborne magnetic and gamma-ray spectrometry data. *SN Appl. Sci.* **2020**, *2*, 1591. https://doi.org/10.1007/s42452-020-03435-1.
84. Mutele, L.; Carranza, E.J.M. Modulated mineral prospectivity mapping of orogenic gold mineralization, Pietersburg Greenstone Belt, South Africa: Exploration targeting from a mineral systems approach. *Nat. Resour. Res.* **2026**, *35*, 877–900. https://doi.org/10.1007/s11053-025-10595-7.
85. Carranza, E.J.M.; Hale, M. Spatial association of mineral occurrences and curvilinear geological features. Math. Geol. 2002, 34, 203–221. https://doi.org/10.1023/A:1014416319335.
86. Eldosouky, A.M.; Abd El Wahed, M.A.; Saada, M.A.; Attia, S.A. New insights into structural and tectonic evolution of Safaga-Semna shear belt, Eastern Desert, Egypt: Advanced integration of aeromagnetic, remote sensing and field studies. *Geomech. Geophys. Geo-Energy Geo-Resour.* **2025**, *11*, 31. https://doi.org/10.1007/s40948-025-00946-2.
87. Abd El Wahed, M.A.; Kamh, S.; Attia, M.; Eldosouky, A.M. Structural geometry and gold ores along the first outlined N–S dextral shear zone in the Egyptian Nubian Shield, East African orogenic belt: New insights from integrated remote sensing, gravity, magnetic and field studies. *Geomech. Geophys. Geo-Energy Geo-Resour.* **2025**, *11*, 76. https://doi.org/10.1007/s40948-025-01003-8.
88. Abd El Wahed, M.A.; Eldosouky, A.M. Characterization of newly identified N–S shear zones in the Egyptian Nubian Shield by integrating geophysical, remote sensing and field data. *Sci. Rep.* **2026**, *16*, 16145. https://doi.org/10.1038/s41598-026-46327-x.
89. Eldosouky, A.M.; Pham, L.T.; El-Qassas, R.A.; Kieu, T.D.; Mohamed, H.; Le, C.V.A. Geophysical data for mineral exploration. In *Geospatial Analysis Applied to Mineral Exploration*; Elsevier: Amsterdam, The Netherlands, 2023; pp. 189–231. https://doi.org/10.1016/B978-0-323-95608-6.00005-6.
90. Ekwok, S.E.; George, A.M.; Omori, A.A.; Abdelrahman, K.; Ugar, S.I.; Andráš, P.; Morphy, M.I.; Akpan, A.E.; Eldosouky, A.M. Unveiling the mineral resources and structural patterns in the Middle Benue Trough: A comprehensive exploration using airborne magnetic and radiometric data. *Geocarto Int.* **2024**, *39*, 2339290. https://doi.org/10.1080/10106049.2024.2339290.
91. Idrus, A.; Kolb, J.; Meyer, F.M. Mineralogy, Lithogeochemistry and Elemental Mass Balance of the Hydrothermal Alteration Associated with the Gold-rich Batu Hijau Porphyry Copper Deposit, Sumbawa Island, Indonesia. *Resour. Geol.* **2009**, *59*, 215–230. https://doi.org/10.1111/j.1751-3928.2009.00092.x.
92. Hassan, S.M.; Youssef, M.A.S.; Gabr, S.; Sadek, M.F. Radioactive mineralization detection using remote sensing and airborne gamma-ray spectrometry at Wadi Al-Miyah, Central Eastern Desert, Egypt. *Egypt. J. Remote Sens. Space Sci.* **2021**, *25*, 37–53. https://doi.org/10.1016/j.ejrs.2021.12.004.
93. Zoheir, B.A.; Akawy, A. Genesis of the Abu Marawat gold deposit, Central Eastern Desert of Egypt. *J. Afr. Earth Sci.* **2010**, *57*, 306–320. https://doi.org/10.1016/j.jafrearsci.2009.10.002.

94. Stern, R.J. The Najd fault system, Saudi Arabia and Egypt: A late Precambrian rift-related transform system? *Tectonics* **1985**, *4*, 497–511.
95. Saada, S.A.; Eleraki, M.; Mansour, A.; Eldosouky, A.M. Insights on the structural framework of the Egyptian Eastern Desert derived from edge detectors of gravity data. *Interpretation* **2025**, *13*, T71–T85. https://doi.org/10.1190/INT-2024-0023.1.
96. El-Sadek, M.A. Radiospectrometric and magnetic signatures of a gold mine in Egypt. *J. Appl. Geophys.* **2009**, *67*, 34–43.

Disclaimer/Publisher's Note: The statements, opinions and data contained in all publications are solely those of the individual author(s) and contributor(s) and not of MDPI and/or the editor(s). MDPI and/or the editor(s) disclaim responsibility for any injury to people or property resulting from any ideas, methods, instructions or products referred to in the content.